Journal Pre-proof

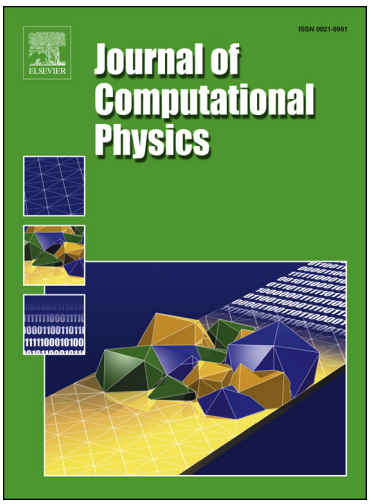

On the evaluation of quasi-periodic Green functions and wave-scattering at and around Rayleigh-Wood anomalies

Oscar P. Bruno, Agustin G. Fernandez-Lado

PII: S0021-9991(20)30126-1
DOI: https://doi.org/10.1016/j.jcp.2020.109352
Reference: YJCPH 109352

To appear in: *Journal of Computational Physics*

Received date: 28 August 2019
Revised date: 6 February 2020
Accepted date: 17 February 2020

Please cite this article as: O.P. Bruno, A.G. Fernandez-Lado, On the evaluation of quasi-periodic Green functions and wave-scattering at and around Rayleigh-Wood anomalies, *J. Comput. Phys.* (2020), 109352, doi: https://doi.org/10.1016/j.jcp.2020.109352.

Highlights

- General, full-spectrum, well-conditioned, Green-function methodology
- Applicable even at and around Wood anomalies
- General quasi-periodic scattering structures, including particle arrays and scattering surfaces in two- and three-dimensional space
- Fast and highly-accurate quasi-periodic solvers for quasi-periodic problems in two and three dimensions including one dimension of periodicity in two dimensions, and either one or two directions of periodicity in three dimensions.

On the evaluation of quasi-periodic Green functions and wave-scattering at and around Rayleigh-Wood anomalies

Oscar P. Bruno* Agustin G. Fernandez-Lado*

Abstract

This article presents full-spectrum, well-conditioned, Green-function methodologies for evaluation of scattering by general periodic structures, which remains applicable on a set of challenging singular configurations, usually called Rayleigh-Wood (RW) anomalies (at which the quasi-periodic Green function ceases to exist), where most existing quasi-periodic solvers break down. After reviewing a variety of existing fast-converging numerical procedures commonly used to compute the classical quasi-periodic Green-function, the present work explores the difficulties they present around RW-anomalies and introduces the concept of hybrid "spatial/spectral" representations. Such expressions allow both the modification of existing methods to obtain convergence at RW-anomalies as well as the application of a slight generalization of the Woodbury-Sherman-Morrison formulae together with a limiting procedure to bypass the singularities. (Although, for definiteness, the overall approach is applied to the scalar (acoustic) wave-scattering problem in the frequency domain, the approach can be extended in a straightforward manner to the harmonic Maxwell's and elasticity equations.) Ultimately, this thorough study of RW-anomalies yields fast and highly-accurate solvers, which are demonstrated with a variety of simulations of wave-scattering phenomena by arrays of particles, crossed impenetrable and penetrable diffraction gratings and other related structures. In particular, the methods developed in this article can be used to "upgrade" classical approaches, resulting in algorithms that are applicable throughout the spectrum, and it provides new methods for cases where previous approaches are either costly or fail altogether. In particular, it is suggested that the proposed shifted Green function approach may provide the only viable alternative for treatment of three-dimensional high-frequency configurations with either one or two directions of periodicity. A variety of computational examples are presented which demonstrate the flexibility of the overall approach.

1 Introduction

Wave-scattering by periodic media, including RW anomalous configurations, at which the quasi-periodic Green function ceases to exist, has continued to attract significant attention in the fields of optics [17, 22, 33, 34, 35, 36, 39, 45, 50] and computational electromagnetism [3, 8, 4, 9, 10, 31, 14, 26, 42, 39, 18]. Classical boundary integral equations methods [43, 49, 52] have relied on the quasi-periodic Green function (denoted throughout this work as G_κ^q), which is defined in terms of a slowly converging infinite series (equation (27)). In order to obtain efficient scattering

*Computing and Mathematical Sciences, Caltech, Pasadena, CA 91125, USA

solvers, several alternative representations, with better convergence properties, have been introduced for the evaluation of G^q_κ. These employ either Kummer or Shanks transformations, lattice sums, Laplace-type integrals and, most notably, the Ewald summation method (a thorough review of these methodologies can be found in [27, 28] and references therein). In the last decade, the novel windowed-Green function (WGF) method was introduced and applied to the periodic problem [3, 9] (cf. [38]) obtaining super-algebraic convergent solvers away from RW-anomalies. With the exception of the Ewald method, the convergence properties of these methodologies deteriorate significantly around RW-anomalies which are pervasive in the most challenging three dimensional case.

A subsequent development to the WGF methodology introduced a novel quasi-periodic "shifted" Green function [3, 10] which, like the "classical" (unshifted) quasi-periodic Green function, is also defined in terms of an infinite series but whose general term has a faster –algebraic– decay rate obtained via the introduction of additional spatial poles. This improvement yields a Green-function which, unlike G^q_κ, is well-defined at RW-anomalies. Since it introduces new spatial singularities, this technique was first applied to problems where the domain boundary coincides with the graph of a periodic function. The contribution [4] introduced a slightly different use of the shifted Green function from its original inception which allows for application to more general domains.

In a nutshell, numerical methods which discretize boundary integral equations basically operate by forming a finite linear system of equations and solving it by either direct or iterative methods. As RW-anomalies are approached in the periodic problem, two sources of error in the numerical solution emerge: the most drastic of them corresponds to (1) Poor approximations of G^q_κ, while a more subtle one is related to (2) Ill-conditioning in the system of equations. Whereas both the WGF and Laplace-type integral methods suffer from the first problem, the shifted Green function and Ewald methods do not. In this context, the main contributions of this article include (a) A theoretical understanding of these difficulties, and (b) Computational algorithms which, exploiting the new theory, enable solution of previously essentially intractable problems. Although, for definiteness, the overall approach is applied to the scalar (acoustic) wave-scattering problem in the frequency domain, the approach can be extended in a straightforward manner to the harmonic Maxwell's and elasticity equations.

Through the introduction of the concept of hybrid "spatial/spectral" representations, this work shows that if a representation of G^q_κ is used which displays explicitly all terms that cause the divergence of G^q_κ as RW anomalies are approached, then high-accuracies can be obtained in the evaluation of G^q_κ in very close proximity (to machine precision) of the singular configuration—thus addressing the evaluation difficulty mentioned in point (1) above. Use of such representations, in turn, provide an insight into the ill-conditioning of the resulting linear systems around RW-anomalies mentioned in point (2) above, and they allow us to introduce a regularization technique, which we refer to as the "Woodbury-Sherman-Morrison (WSM) methodology", that resolves the difficulty and can be used to produce solutions at RW-anomalies using quasi-periodic Green function methods. These two elements are the building blocks of the proposed strategy which, ultimately, strives to obtain fast, robust and highly-accurate solvers to simulate wave-scattering phenomena by periodic media in general geometries irrespectively of the occurrence of RW-anomalies.

This paper is organized as follows: after needed background is presented in Section 2, Section 3 introduces certain reformulated expressions for the classical quasi-periodic Green function. The WSM framework we propose is then put forth in Section 4. Section 5, finally, presents a variety of numerical results demonstrating the character of the overall methodology.

2 Preliminaries and notations

2.1 Periodic structures

This article considers frequency-domain problems of wave scattering by periodic penetrable and impenetrable diffraction gratings in two- and three-dimensional space, including arrays of particles, layers of corrugated surfaces and combinations thereof. In all cases the propagation domain $\Omega \subseteq \mathbb{R}^d$ ($d = 2, 3$) is infinite and translationally invariant with respect to a certain periodicity lattice Λ. In detail, calling

$$\Lambda = \left\{ \sum_{i=1}^{d_\Lambda} m_i \boldsymbol{v_i} : m_i \in \mathbb{Z} \right\}, \tag{1}$$

a given d_Λ-dimensional periodicity lattice ($1 \leq d_\Lambda < d$), Ω satisfies the translation-invariance property

$$\Omega + \boldsymbol{R} = \Omega \quad \text{for all} \quad \boldsymbol{R} \in \Lambda. \tag{2}$$

The directions $\boldsymbol{v_i}$, $i = 1, \ldots, d_\Lambda$ in (1) are commonly called the primitive (or periodicity) vectors of the lattice. Without loss of generality, throughout this work it is assumed that $\boldsymbol{v_1}$ is parallel to the x_1-axis, and that the lattice is contained in the subspace generated by the vectors $x_1, \ldots, x_{d_\Lambda}$ (so that the periodicity lattice is contained in the line $\{(x_1, 0)\}$ in two dimensions, and either in the line $\{(x_1, 0, 0)\}$ or the plane $\{(x_1, x_2, 0)\}$ in three dimensions).

Remark 1. In what follows, for $\boldsymbol{x} \in \mathbb{R}^d$ we let $\boldsymbol{x}^\perp$ denote the projection of $\boldsymbol{x}$ into the subspace orthogonal to the set Λ, and we call $\boldsymbol{x}^\parallel = \boldsymbol{x} - \boldsymbol{x}^\perp$. Thus, for $\boldsymbol{x} = (x_1, x_2, x_3)$ we have e.g. $\boldsymbol{x}^\perp = (0, x_2, x_3)$ for $d = 3$ and $d_\Lambda = 1$, while $\boldsymbol{x}^\perp = (0, 0, x_3)$ for $d = 3$ and $d_\Lambda = 2$.

Clearly, the projection $\boldsymbol{x}^\parallel = \boldsymbol{x} - \boldsymbol{x}^\perp$ can be expressed in the form

$$\boldsymbol{x}^\parallel = \sum_{i=1}^{d_\Lambda} a_i \boldsymbol{v_i}, \quad a_i \in \mathbb{R}. \tag{3}$$

and so, letting $\boldsymbol{x}^\sharp = \sum_{i=1}^{d_\Lambda} b_i \boldsymbol{v_i} + \boldsymbol{x}^\perp$ where the coefficients $b_i = a_i - \lfloor a_i \rfloor$ belong to the interval $[0, 1)$, any point $\boldsymbol{x} \in \mathbb{R}^d$ is a translation of $\boldsymbol{x}^\sharp$ by the lattice Λ. In what follows, for any set $S \subseteq \mathbb{R}^d$ we will let $S^\sharp$ denote the set

$$S^\sharp = \left\{ \boldsymbol{x}^\sharp : \boldsymbol{x} \in S \right\}. \tag{4}$$

We say that a set $S \subseteq \mathbb{R}^d$ is *transversely bounded* (resp. *transversely unbounded*) if the corresponding set $S^\sharp$ is bounded (resp. unbounded).

2.2 Scattering problems

For a given incident field u^{inc}, we seek to evaluate the associated acoustic fields under sound-soft and sound-hard conditions. In the sound-soft case, for example, the acoustic field u is solution (in the weak sense) of the scalar Helmholtz equation

$$\Delta u + k^2 n^2(\boldsymbol{x}) u = 0 \quad \text{in } \Omega, \tag{5}$$

with wavenumber $k > 0$, while in the sound-hard case, u satisfies

$$\nabla \cdot \left(\frac{1}{n^2(\boldsymbol{x})} \nabla u \right) + k^2 u = 0 \quad \text{in } \Omega. \tag{6}$$

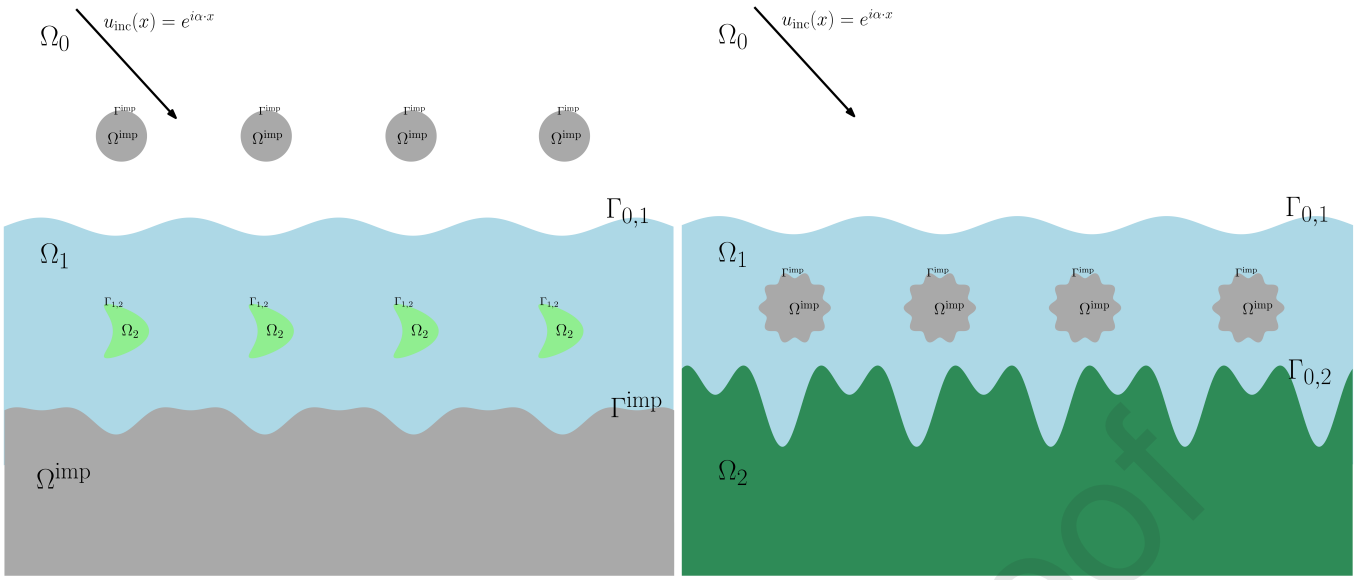

Figure 1: Incoming plane waves impinging on two periodic structures of the types considered in this contribution. In both cases the refractive index assumes three different values and the dark-gray regions indicate the domain Ω^{imp} which waves cannot penetrate. The left figure includes only one transversally unbounded propagation region (Ω_0), while the right figure contains two transversally unbounded regions (Ω_0 and Ω_2). Thus, these examples demonstrate cases where Ω_{r+1} is empty and non-empty, respectively.

Here the refractive-index function $n(\boldsymbol{x}) > 0$ is a Λ-periodic function of $\boldsymbol{x}$ throughout Ω, that is $n(\boldsymbol{x} + \boldsymbol{R}) = n(\boldsymbol{x})$ for all $\boldsymbol{x} \in \Omega$ and all $\boldsymbol{R} \in \Lambda$, and locally constant, with a finite set of values. The propagation domain Ω is decomposed as a finite union

$$\Omega = \bigcup_{j=0}^{r+1} \Omega_j, \tag{7}$$

of the sets $\Omega_0, \Omega_1, \ldots, \Omega_r, \Omega_{r+1}$, on each one of which the refractive index is constant (see Figure 1). In detail, throughout this article it is assumed that

1. All except at most two of the sets Ω_j are transversely bounded. The set Ω_0 is required to be transversely unbounded, and Ω_{r+1} is either transversely unbounded or empty.

2. For $d_\lambda = d - 1$, Ω_0 contains a set of the form $\{x_d > M\}$ for some $M > 0$. For $d = 3$ and $d_\lambda = 1$, Ω_0 contains a set of the form $\{|\boldsymbol{x}^\perp| > M\}$. If $\Omega_{r+1} \neq \emptyset$ (which is not possible for $d = 3$ and $d_\lambda = 1$), then Ω_{r+1} contains the set $\{x_d < -M\}$ for some $M > 0$.

3. There are at most two and at least one transversely-unbounded constant-refractivity sets. One of these sets, denoted by Ω_0, is assumed to contain the incident field. The set denoted by Ω_{r+1} ($r \geq 0$), on the other hand, equals either the second transversely-unbounded constant-refractivity set or, if Ω_0 is the only such set, then $\Omega_{r+1} = \emptyset$.

Using these notations, equations (5) and (6) become

$$\Delta u + k^2 n_j^2 u = 0 \quad \text{in } \Omega_j \quad \text{for } 0 \leq j \leq r+1. \tag{8}$$

Note that Ω may or may not equal the totality of $\mathbb{R}^d$. In the case $\Omega = \mathbb{R}^d$ each portion of space is occupied by a penetrable material. In the case $\Omega \neq \mathbb{R}^d$, in turn, the complement Ω^{imp} of the closure of Ω,

$$\Omega^{\mathrm{imp}} = \mathbb{R}^d \setminus \Omega = \mathbb{R}^d \setminus \left(\bigcup_{j=0}^{r+1} \Omega_j \right)$$

is assumed to be occupied by either sound-soft or sound-hard impenetrable media, or a combination of the two. Thus Ω^{imp} is given by the union

$$\Omega^{\mathrm{imp}} = \Omega_D^{\mathrm{imp}} \cup \Omega_N^{\mathrm{imp}}$$

of the disjoint sets Ω_D^{imp} (with boundary Γ_D^{imp}) and Ω_N^{imp} (with boundary Γ_N^{imp}) occupied by sound-soft and sound-hard materials, respectively:

$$\Gamma^{\mathrm{imp}} = \Gamma_D^{\mathrm{imp}} \cup \Gamma_N^{\mathrm{imp}}$$

For simplicity, throughout this contribution it is assumed that Γ_D^{imp} and Γ_N^{imp} are disjoint, but the general non-disjoint case can also be considered within this context (cf. [1]).

We assume that the structure is illuminated by a plane wave u^{inc} defined in the transversely-unbounded domain Ω_0, where

$$u^{\mathrm{inc}}(\boldsymbol{x}) = \mathrm{e}^{\mathrm{i}\boldsymbol{\alpha}\cdot\boldsymbol{x} - \mathrm{i}\boldsymbol{\beta}\cdot\boldsymbol{x}}, \quad \boldsymbol{x} \in \Omega_0. \tag{9}$$

Here $\boldsymbol{\alpha}$ and $\boldsymbol{\beta}$ are parallel and perpendicular to the lattice Λ, respectively, and verify $|\boldsymbol{\alpha}|^2 + |\boldsymbol{\beta}|^2 = n_0^2 k^2$; the scattered field u^{s} is thus defined by the relations

$$u^{\mathrm{s}}(\boldsymbol{x}) = \begin{cases} u(\boldsymbol{x}) - u^{\mathrm{inc}}(\boldsymbol{x}), & \boldsymbol{x} \in \Omega_0 \\ u(\boldsymbol{x}), & \boldsymbol{x} \in \Omega_j,\ j \geq 1 \end{cases} \tag{10}$$

and we clearly have

$$\Delta u^{\mathrm{s}} + k^2 n_j^2 u^{\mathrm{s}} = 0 \quad \text{in } \Omega_j \quad \text{for } 0 \leq j \leq r+1. \tag{11}$$

For each pair j, ℓ of indices, $j < \ell$, we denote by $\Gamma_{j\ell}$ the boundary between Ω_j and Ω_ℓ, and we let $\Gamma_{j\ell} = \emptyset$ for $j \geq \ell$. For $\boldsymbol{x} \in \Gamma_{j\ell}$ $(j < \ell)$, $\nu = \nu(\boldsymbol{x})$ denotes the unit normal vector to $\Gamma_{j\ell}$ which points into the "plus side" Ω_j of $\Gamma_{j\ell}$. (Note that, even for $j < \ell$, $\Gamma_{j\ell}$ is empty whenever Ω_j and Ω_ℓ do not share a common boundary.) For $\boldsymbol{x} \in \Gamma^{\mathrm{imp}}$, in turn, $\nu = \nu(\boldsymbol{x})$ denotes the normal to Γ^{imp} which points into the interior of Ω (or into the exterior of Ω^{imp}). Additionally we define the set of all points at transmission boundaries (resp. all points at impenetrable boundaries) by $\Gamma^{\mathrm{trans}} = \bigcup_{j<\ell} \Gamma_{j\ell}$ (resp. $\Gamma^{\mathrm{imp}} = \partial\Omega$), and we call $\Gamma = \Gamma^{\mathrm{trans}} \cup \Gamma^{\mathrm{imp}}$ the set of all points at interface boundaries. The impenetrable boundary Γ^{imp} may additionally be decomposed into its sound-hard and sound-soft portions: $\Gamma^{\mathrm{imp}} = \Gamma_s^{\mathrm{imp}} \cup \Gamma_h^{\mathrm{imp}}$. For $\boldsymbol{x} \in \Gamma$ we define the boundary values of a function u and its normal derivative at $\boldsymbol{x}$ from the $+$ and $-$ sides of an interface by

$$u_\pm(\boldsymbol{x}) = \lim_{\delta \to 0^+} \big[u(\boldsymbol{x} \pm \delta\nu(\boldsymbol{x})) \big] \quad \text{and} \quad \frac{\partial u_\pm}{\partial \nu}(\boldsymbol{x}) = \lim_{\delta \to 0^+} \big[\nabla u(\boldsymbol{x} \pm \delta\nu(\boldsymbol{x})) \cdot \nu(\boldsymbol{x}) \big]. \tag{12}$$

The PDE problem under consideration is fully determined by equation (8) together with the boundary conditions

$$u = 0 \quad \text{for} \quad \boldsymbol{x} \in \Gamma_s^{\mathrm{imp}} \quad \text{and} \quad \frac{\partial u}{\partial \nu} = 0 \quad \text{for} \quad \boldsymbol{x} \in \Gamma_h^{\mathrm{imp}}, \tag{13}$$

together with the transmission conditions

$$u_+ - u_- = 0 \quad \text{and} \quad \frac{\partial u_+}{\partial \nu} - \frac{1}{C_{j\ell}^2}\frac{\partial u_-}{\partial \nu} = 0, \quad \boldsymbol{x} \in \Gamma_{j\ell} \tag{14}$$

and the conditions of radiation at infinity. (The latter concept, together with the related reciprocal lattice Λ^* and the associated Rayleigh expansion, are described in what follows.) In these equations we have set

$$C_{j\ell} = \begin{cases} 1 & \text{in the sound-soft case, and} \\ \frac{n_\ell}{n_j} & \text{in the sound-hard case.} \end{cases}$$

The reciprocal lattice

$$\Lambda^* = \left\{ \sum_{j=1}^{d_\Lambda} m_j \boldsymbol{w_j} : m_j \in \mathbb{Z} \right\} \tag{15}$$

plays an important role in the context of periodic lattice sums we consider—which can be represented either as series with support over the lattice Λ or, on account of the Poisson summation formula [47], over the reciprocal lattice Λ^*. The reciprocal basis vectors $\boldsymbol{w_j}$, $j = 1, \ldots, d_\Lambda$, are defined as the vectors which span the same vector subspace as the set $\{\boldsymbol{v_i} : i = 1, \ldots, d_\Lambda\}$, and which verify the relations

$$\boldsymbol{v_i} \cdot \boldsymbol{w_j} = 2\pi \delta_i^j. \tag{16}$$

Following [27], using the multi-index $\boldsymbol{m} = (m_1, \ldots, m_{d_\Lambda}) \in \mathbb{Z}^{d_\Lambda}$, elements of Λ and Λ^* will be denoted by

$$\boldsymbol{R_m} = \sum_{i=1}^{d_\Lambda} m_i \boldsymbol{v_i} \quad \text{and} \quad \boldsymbol{K_m} = \sum_{i=1}^{d_\Lambda} m_i \boldsymbol{w_i}, \tag{17}$$

respectively.

We say that a function u defined on Ω is $\boldsymbol{\alpha}$-quasi-periodic with respect to Λ provided

$$u(\boldsymbol{x} + \boldsymbol{R_m}) = \mathrm{e}^{\mathrm{i}\boldsymbol{\alpha}\cdot\boldsymbol{R_m}} u(\boldsymbol{x}) \quad \text{for all} \quad \boldsymbol{m} \in \mathbb{Z}^{d_\Lambda}. \tag{18}$$

Clearly, the incident field (9) is an $\boldsymbol{\alpha}$-quasi-periodic function and, as is well known [43], so is the scattered field u^s. On any set of the form

$$V_{m_1}^{m_2} = \{\boldsymbol{x} \in \mathbb{R}^d : m_1 < |\boldsymbol{x}^\perp| < m_2\} \tag{19}$$

that satisfies

$$V_{m_1}^{m_2} \subseteq \Omega_j \quad \text{for some} \quad j, \tag{20}$$

the solution u^{s} in (11) (like any quasi-periodic solution of the Helmholtz equation) may be expressed as an $\boldsymbol{\alpha}$-quasi-periodic *Rayleigh-series* expansion of the form

$$u^{\mathrm{s}}(\boldsymbol{x}) = \sum_{\boldsymbol{m}\in\mathbb{Z}^{d_\Lambda}} A_{\boldsymbol{m}}^{+} \mathrm{e}^{\mathrm{i}\boldsymbol{\alpha_m}\cdot\boldsymbol{x} + \mathrm{i}\beta_{\boldsymbol{m}}(n_j k)x_d} + A_{\boldsymbol{m}}^{-} \mathrm{e}^{\mathrm{i}\boldsymbol{\alpha_m}\cdot\boldsymbol{x} - \mathrm{i}\beta_{\boldsymbol{m}}(n_j k)x_d}, \quad d_\Lambda = d - 1 \tag{21}$$

and

$$u^{\mathrm{s}}(\boldsymbol{x}) = \sum_{\boldsymbol{m}\in\mathbb{Z}^{d_\Lambda}} \mathrm{e}^{\mathrm{i}\boldsymbol{\alpha_m}\cdot\boldsymbol{x}} U_{\boldsymbol{m}}(x_2, x_3) \quad d_\Lambda = 1, d = 3, \tag{22}$$

where $U_{\boldsymbol{m}}(x_2, x_3)$ satisfies the Helmholtz equation with wavenumber $\beta_{\boldsymbol{m}}(n_j k)$ in two-dimensional space

$$\Delta U_{\boldsymbol{m}}(x_2, x_3) + \beta_{\boldsymbol{m}}(n_j k)^2 U_{\boldsymbol{m}}(x_2, x_3) = 0. \tag{23}$$

In (21) and (22) we have set

$$\boldsymbol{\alpha_m} = \boldsymbol{\alpha} + \boldsymbol{K_m}, \quad \beta_{\boldsymbol{m}} = \beta_{\boldsymbol{m}}(\kappa) = \sqrt{\kappa^2 - |\boldsymbol{\alpha_m}|^2} \quad \text{and} \quad \mathrm{Im}(\beta_{\boldsymbol{m}}) \geq 0. \tag{24}$$

Remark 2. Throughout this work we consider problems for which the propagation domain Ω extends to infinity both along the periodic lattice direction as well as along orthogonal directions to the lattice (see points 1–3 above in the present section. Note that in the case $d_\Lambda = d - 1$, the modes $\mathrm{e}^{\mathrm{i}\boldsymbol{\alpha_m}\cdot\boldsymbol{x}+\mathrm{i}\beta_{\boldsymbol{m}}x_d}$ and $\mathrm{e}^{\mathrm{i}\boldsymbol{\alpha_m}\cdot\boldsymbol{x}-\mathrm{i}\beta_{\boldsymbol{m}}x_d}$ represent outgoing waves in the half-spaces $x_d > M$ and $x_d < -M$ respectively. Similarly, the cylindrical waves $\mathrm{e}^{\mathrm{i}\boldsymbol{\alpha_m}\cdot\boldsymbol{x}} H_0^{(1)}\left(\beta_{\boldsymbol{m}}\sqrt{x_2^2 + x_3^2}\right)$ represent outgoing waves in the case $d_\Lambda = 1$, $d = 3$. A quasi-periodic solution of the Helmholtz equation (8) is called radiating if the relevant associated Rayleigh expansion, either (21) or (22), only contains outgoing modes in any set $V_{m_1}^{m_2}$ satisfying (20). Thus the scattered field u^{s}, which has been assumed to be radiating, i.e., it only contains outgoing modes and remains bounded as $|\boldsymbol{x}^\perp| \to \infty$, is given by a Rayleigh expansion of the form

$$u^{\mathrm{s}}(\boldsymbol{x}) = \sum_{\boldsymbol{m}\in\mathbb{Z}^{d_\Lambda}} A_{\boldsymbol{m}}^{+}\mathrm{e}^{\mathrm{i}\boldsymbol{\alpha_m}\cdot\boldsymbol{x}+\mathrm{i}\beta_{\boldsymbol{m}}(n_j k)x^\perp}, \quad x_d > M \quad \text{and} \quad \sum_{\boldsymbol{m}\in\mathbb{Z}^{d_\Lambda}} A_{\boldsymbol{m}}^{-}\mathrm{e}^{\mathrm{i}\boldsymbol{\alpha_m}\cdot\boldsymbol{x}-\mathrm{i}\beta_{\boldsymbol{m}}(n_j k)x^\perp}, \quad x_d < -M \tag{25}$$

if $d_\Lambda = d - 1$ and

$$u^{\mathrm{s}}(\boldsymbol{x}) = \sum_{\boldsymbol{m}\in\mathbb{Z}^{d_\Lambda}} \mathrm{e}^{\mathrm{i}\boldsymbol{\alpha_m}\cdot\boldsymbol{x}} U_{\boldsymbol{m}}(x_2, x_3) \tag{26}$$

if $d_\Lambda = 1$, $d = 3$ where $U_{\boldsymbol{m}}(x_2, x_3)$ satisfies (23) and the two-dimensional Sommerfeld radiation condition [16, Eqn. 3.85].

We will obtain $\boldsymbol{\alpha}$-quasi-periodic solutions of equation (8) by relying on integral equations and $\boldsymbol{\alpha}$-quasi-periodic Green functions. The classical $\boldsymbol{\alpha}$-quasi-periodic Green function is introduced in the following section, which additionally describes the difficulties that arise at Rayleigh-Wood anomalies. (Section 4.2 presents a new strategy leading to Green-function solutions even at and around Wood anomalies.)

2.3 Quasi-periodic Green function

Given $\boldsymbol{\alpha} \in \mathbb{R}^d$ and $\kappa > 0$ the quasi-periodic Green function G_κ^q is given by the conditionally-convergent sum

$$G_\kappa^q(\boldsymbol{x}) = \sum_{\boldsymbol{m}\in\mathbb{Z}^{d_\Lambda}} \mathrm{e}^{\mathrm{i}\boldsymbol{\alpha}\cdot\boldsymbol{R_m}} G_\kappa(\boldsymbol{x} - \boldsymbol{R_m}) \tag{27}$$

where

$$G_\kappa(\boldsymbol{x}) = \begin{cases} \frac{\mathrm{i}}{4} H_0^{(1)}(\kappa|\boldsymbol{x}|) & \text{for } d = 2, \\ \frac{1}{4\pi}\frac{\mathrm{e}^{\mathrm{i}\kappa|\boldsymbol{x}|}}{|\boldsymbol{x}|} & \text{for } d = 3 \end{cases} \tag{28}$$

denotes the free-space Green function for the Helmholtz equation with wavenumber κ in d-dimensional space.

The quasi-periodic Green function can be interpreted as the field generated by an infinite number of radiating point sources distributed periodically and acting coherently through a suitable phase factor. A direct application of the Poisson summation formula to (27) yields the corresponding spectral representations for the quasi-periodic Green function:

$$G_\kappa^q(\boldsymbol{x}) = \frac{1}{\mathcal{A}}\frac{\mathrm{i}}{2}\sum_{\boldsymbol{m}\in\mathbb{Z}^{d_\Lambda}} \frac{\mathrm{e}^{\mathrm{i}\boldsymbol{\alpha}_{\boldsymbol{m}}\cdot\boldsymbol{x}}\mathrm{e}^{\mathrm{i}\beta_{\boldsymbol{m}}|x_d|}}{\beta_{\boldsymbol{m}}}, \quad d=2,3 \quad \text{and} \quad d_\lambda = d-1 \tag{29}$$

$$G_\kappa^q(\boldsymbol{x}) = \frac{1}{\mathcal{A}}\frac{\mathrm{i}}{4}\sum_{\boldsymbol{m}\in\mathbb{Z}^{d_\Lambda}} \mathrm{e}^{\mathrm{i}\boldsymbol{\alpha}_{\boldsymbol{m}}\cdot\boldsymbol{x}} H_0^{(1)}\left(\beta_{\boldsymbol{m}}\sqrt{x_2^2+x_3^2}\right), \quad d=3, d_\lambda = 1. \tag{30}$$

Here $\mathcal{A}$ denotes the area of the unit cell,

$$\mathcal{A} = \begin{cases} |\boldsymbol{v_1}| & \text{if } d_\lambda = 1 \\ |\boldsymbol{v_1}\times\boldsymbol{v_2}| & \text{if } d_\lambda = 2 \end{cases} \tag{31}$$

and the parameters $\boldsymbol{\alpha}_{\boldsymbol{m}}$ and $\beta_{\boldsymbol{m}}$ are defined in (24). The spectral representations (29) through (30) manifest the singular character of the quasi-periodic Green function at configurations for which the scalar $\beta_{\boldsymbol{m}}$ vanishes for some value or (finite number of) values of the index $\boldsymbol{m}$: as such singular configurations are approached, singularities of type $\beta_{\boldsymbol{m}}^{-1}$ and $\log(\beta_{\boldsymbol{m}})$ arise for $d = d_\Lambda + 1$ and $d = d_\Lambda + 2$, respectively. A triple $(\kappa, \boldsymbol{\alpha}, \Lambda)$ for which $\beta_{\boldsymbol{m}}$ vanishes for some value of $\boldsymbol{m}$ is said to be a Rayleigh-Wood (RW) anomaly triple; clearly, at RW anomalies the (finite) set

$$\mathcal{W}(\kappa, \boldsymbol{\alpha}, \Lambda) = \left\{\boldsymbol{m}\in\mathbb{Z}^{d_\Lambda} : \kappa^2 - |\boldsymbol{\alpha}+\boldsymbol{K}_{\boldsymbol{m}}|^2 = 0\right\} = \left\{\boldsymbol{m}\in\mathbb{Z}^{d_\Lambda} : \beta_{\boldsymbol{m}} = 0\right\} \tag{32}$$

is non-empty.

The spectral representations (29) and (30) provide an exceptional computational tool whenever the following conditions are satisfied: 1) The triple $(\kappa, \boldsymbol{\alpha}, \Lambda)$ is not a RW anomaly; and 2) The magnitude $|\boldsymbol{x}^\perp|$ of the projection $\boldsymbol{x}^\perp$ is relatively large compared to the wavelength—since, in such cases, the series (29) and (30) converge exponentially fast to the corresponding quasi-periodic Green functions. For small values of $|\boldsymbol{x}^\perp|$, however, the convergence rates deteriorates. To compute the quasi-periodic Green functions in the latter regime alternative representations must be used which, like the one displayed in equation (27), make explicit the spatial Green-function singularities. The representation (27) is only conditionally convergent, however, and therefore finite truncations of it yield poor approximations. For example, a straightforward truncation in the $d_\Lambda = 1$ case converges with an error that decays like the inverse of the square root of the numbers of terms used.

A number of methodologies have been developed which, for configurations away from RW anomalies, can be used to evaluate the quasi-periodic Green function efficiently and accurately—including lattice sums [18, 27, 28], Laplace-type integral representation [6, 7, 23, 24, 52], the Ewald summation method [2, 12, 20, 27, 40] and, recently, the Windowed Green function (WGF) method [3, 9]. (In fact the WGF method yields algebraic high-order convergence even at RW anomalies when used in conjunction with the shifted Green function [3, 8, 9]). Except for the shift-based Green function approach, however, all of these methodologies fail at RW anomalies since the classical quasi-periodic Green function is not even defined in that case. (For an exact solution for a periodic array of circular scatterers in two-dimensional space, reference [30] shows that the solution tends to a limit as an RW anomaly is approached.) Section 3 describes the integral, Ewald and shifted Green function approaches, each one of which can be used as a basis for a RW-anomaly strategy—as indicated in Section 4.

3 Jointly spatial-spectral quasi-periodic Green function representations

3.1 Laplace-type integral method ($d_\Lambda = 1$)

In the case $d_\Lambda = 1$, Laplace transform methods can be used to express the quasi-periodic Green functions as a sum of a single free-space Green function and certain Laplace-type integrals. Laplace-type Integral methods have been successfully extended to bi-periodic arrays, $d_\Lambda = 2$, for Cartesian lattices [27]—for which the generating vectors $\boldsymbol{v_1}$ and $\boldsymbol{v_2}$ are orthogonal—but we do not consider such extensions in this work. A full description of the $d_\Lambda = 1$ methods can be found in [23, 24, 27, 28, 52]. Assuming $\boldsymbol{v_1} = L\hat{\boldsymbol{x}}_{\boldsymbol{1}}$ (L is the period of the lattice) the Laplace-type integral representation of the classical quasi-periodic Green function (27) in the case $d_\Lambda = 1$ is given by

$$G^q_\kappa(\boldsymbol{x}) = G_\kappa(\boldsymbol{x}) + \frac{\mathrm{e}^{-\mathrm{i}\kappa\boldsymbol{x}\cdot\hat{\boldsymbol{e}}}}{2\pi} I^+(\boldsymbol{x}) + \frac{\mathrm{e}^{\mathrm{i}\kappa\boldsymbol{x}\cdot\hat{\boldsymbol{e}}}}{2\pi} I^-(\boldsymbol{x}) \tag{33}$$

where

$$I^\pm(\boldsymbol{x}) = \int_0^\infty \frac{\mathrm{e}^{-\kappa(L\pm x_1)u}}{\mathrm{e}^{-\mathrm{i}(\kappa\mp\boldsymbol{\alpha}\cdot\hat{\boldsymbol{x}}_{\boldsymbol{1}})L} - \mathrm{e}^{-\kappa L u}} \frac{f_d\left(\kappa|\boldsymbol{x}^\perp|\sqrt{u^2 - 2\mathrm{i}u}\right)}{(u^2 - 2\mathrm{i}u)^{(3-d)/2}} du \tag{34}$$

and

$$f_d(t) = \cos(t) \quad \text{for } d = 2 \quad \text{and} \quad f_d(t) = \frac{\kappa}{2} J_0(t) \quad \text{for } d = 3. \tag{35}$$

The generalized Gauss-Laguerre quadrature rule [44] is well suited for evaluation of the integrals $I^\pm$. In contrast to the spectral representations, formula (33) makes explicit the spatial singularity around the origin of the quasi-periodic Green function but it does not present in a similarly explicit form the singularity at RW anomalies—which is explicit in (29) and (30). The Laplace-type integral representation (33), which was used in [6, 7] to produce efficient periodic scattering solvers for challenging configurations, is also a key component in the analysis performed in [23, 24] for the periodic problem at high frequencies. The strategies presented in all of these references are not applicable at RW anomalies, however.

As detailed in what follows, each of the integrals $I^\pm$ can be re-expressed as a sum of two terms: a first one which explicitly captures the RW-anomaly singularities in (29) and (30), and a second one which is given by a rapidly convergent integral, and which remains bounded near RW anomalies. To see this we first note that, except at RW-anomalies the denominator $\mathrm{e}^{-\mathrm{i}(\kappa\mp\boldsymbol{\alpha}\cdot\hat{\boldsymbol{x}}_{\boldsymbol{1}})L} - \mathrm{e}^{-\kappa L u}$ in (34) does not vanishes in the integration domain. Indeed, the zeroes of the denominator are the purely imaginary numbers $\mathrm{i}u^\pm_m$, where

$$\kappa u^\pm_m = \kappa \mp \boldsymbol{\alpha_m} \cdot \hat{\boldsymbol{x}}_{\boldsymbol{1}}, \tag{36}$$

Clearly these zeroes can only be real if $\kappa u^\pm_m$ vanishes, or, equivalently, if the RW-anomaly condition $|\boldsymbol{\alpha_m}| = \kappa$ is satisfied. In particular, at RW-anomalies, at least one of the integrals $I^\pm$ diverges.

In order to explicitly extract the singular term we multiply and divide the integrand in (34) by $u - \mathrm{i}u^\pm_m$ and we obtain

$$I^\pm(\boldsymbol{x}) = \int_0^\infty \frac{\mathrm{e}^{-\kappa(L\pm x_1)u}}{u - \mathrm{i}u^\pm_m} \frac{1}{u^{(3-d)/2}} g_d(u) du \tag{37}$$

where we have set

$$g_d(u) = \frac{u - \mathrm{i}u_m^{\pm}}{\mathrm{e}^{-\mathrm{i}(\boldsymbol{\alpha}\cdot\boldsymbol{\hat{x}_1}\mp\kappa)L} - \mathrm{e}^{-\kappa L u}} \frac{f_d\left(\kappa|\boldsymbol{x}^{\perp}|\sqrt{u^2 - 2\mathrm{i}u}\right)}{(u - 2\mathrm{i})^{(3-d)/2}}.$$

As a function of the real variable u, g_d is an infinitely differentiable function around the origin (since in either case, $d = 2$ and $d = 3$, the Taylor series of the analytic function f_d around zero only contains even powers). Adding and subtracting $g_d(\mathrm{i}u_m^{\pm})$ from $g_d(u)$ in (37) we obtain

$$I^{\pm}(\boldsymbol{x}) = \int_0^{\infty} \frac{\mathrm{e}^{-\kappa(L\pm x_1)u}}{u^{(3-d)/2}} \frac{g_d(u) - g_d(\mathrm{i}u_m^{\pm})}{u - \mathrm{i}u_m^{\pm}} du + g_d(\mathrm{i}u_m^{\pm}) \int_0^{\infty} \frac{\mathrm{e}^{-\kappa(L\pm x_1)u}}{u - \mathrm{i}u_m^{\pm}} \frac{du}{u^{(3-d)/2}}. \tag{38}$$

Clearly, the integrand in the first term of the right hand side of equation (38) is regular and can be evaluated by means of the Gauss-Laguerre quadrature rule. The last integral on the right-hand side, in turn, can be expressed in terms of special functions. Indeed, in the case $d = 2$ using the relation [19, Eq. 7.7.2]

$$\mathrm{e}^{-z^2}\mathrm{erfc}\left(-\mathrm{i}z\right) = \frac{z}{\pi\mathrm{i}} \int_{-\infty}^{\infty} \frac{\mathrm{e}^{-t^2}}{t^2 - z^2} dt, \quad \mathrm{Im}(z) > 0 \tag{39}$$

and the change of variables $u = t^2$ we obtain

$$\int_0^{\infty} \frac{\mathrm{e}^{-\kappa(L\pm x_1)u}}{u - \mathrm{i}u_m^{\pm}} \frac{du}{\sqrt{u}} = \pi \mathrm{e}^{\mathrm{i}\pi/4} \mathrm{e}^{-\mathrm{i}\kappa u_m^{\pm}(L\pm x_1)} \frac{\mathrm{erfc}\left(\mathrm{e}^{-\mathrm{i}\pi/4}\sqrt{\kappa u_m^{\pm}(L \pm x_1)}\right)}{\sqrt{u_m^{\pm}}} \tag{40}$$

where erfc denotes the analytic extension of the complementary error function

$$\mathrm{erfc}(z) = \frac{2}{\sqrt{\pi}} \int_z^{\infty} \mathrm{e}^{-t^2} dt \tag{41}$$

to the complex plane. For the case $d = 3$, in turn, we have

$$\int_0^{\infty} \frac{\mathrm{e}^{-\kappa(L\pm x_1)u}}{u - \mathrm{i}u_m^{\pm}} du = \mathrm{e}^{-\mathrm{i}\kappa u_m^{\pm}(L\pm x_1)} E_1\left(-\mathrm{i}\kappa u_m^{\pm}(L \pm x_1)\right) \tag{42}$$

where E_1 denotes the analytic extension of the exponential integral

$$E_1(z) = \int_z^{\infty} \frac{\mathrm{e}^{-t}}{t} dt$$

to the maximal analyticity domain $\mathbb{C} \setminus (-\infty, 0]$ (that is also commonly used as the principal branch of the logarithm function). The factor $g_d(\mathrm{i}u_m)$ that multiplies the last integral on the right-hand side of equation (38) (in either case, $d = 2$ or $d = 3$) in turn, is given by

$$g_d(\mathrm{i}u_m) = \frac{\mathrm{e}^{\mathrm{i}\kappa L u_m^{\pm}}}{\kappa L} \frac{f_d\left(\kappa|\boldsymbol{x}^{\perp}|\sqrt{2u_m - u_m^2}\right)}{(\mathrm{i}(u_m - 2))^{(3-d)/2}}, \tag{43}$$

as it can be checked easily. In view of equations (40), (42) and (43) together with the relation $\beta_m(\kappa) = \kappa\sqrt{2u_m - u_m^2}$ (that results from (24) and (36)) it follows that the second term on the right hand side of (38) equals

$$\pi \frac{\mathrm{i}}{L} \mathrm{e}^{\mp \mathrm{i}\kappa u_m^{\pm} x_1} \mathrm{erfc}\left(\mathrm{e}^{-\mathrm{i}\pi/4}\sqrt{\kappa u_m^{\pm}(L \pm x_1)}\right) \frac{\cos\left(\beta_m(\kappa)|\boldsymbol{x}^{\perp}|\right)}{\beta_m(\kappa)} \tag{44}$$

for $d = 2$ and

$$\frac{1}{2L} \mathrm{e}^{\mp \mathrm{i}\kappa u_m^{\pm} x_1} J_0\left(\beta_m(\kappa)|\boldsymbol{x}^{\perp}|\right) E_1\left(-\mathrm{i}\frac{\beta_m(\kappa)^2}{\kappa + \sqrt{\kappa^2 - \beta_m(\kappa)^2}}(L \pm x_1)\right) \tag{45}$$

for $d = 3$. In either the case $d = 2$ or $d = 3$, substituting the last integral in equation (38) by the corresponding expression (44) or (45), and then replacing the ensuing formulae for $I^{\pm}$ into (33), yields an expression for the quasi-periodic Green function G_κ^q in terms of special functions and integrals that do not suffer from singularity at RW-anomalies. The $1/\beta_m$ Green-function singularity in the case $d = 2$ is explicitly displayed in (44), while the corresponding logarithmic singularity in the case $d = 3$ can be made explicit by using the relation [19, Eq. 6.6.2]

$$E_1(z) = -C - \log(z) - \sum_{k=1}^{\infty} \frac{(-z)^k}{k \cdot k!}. \tag{46}$$

The special-function values required to evaluate the expressions (44) and (45) can generally be obtained without difficulty by means of well known algorithms. As discussed in [23, 24], however, the necessary integrals (namely, the first integral expression on the right-hand side in (38) for $d = 2$ and $d = 3$), while regular at RW-anomalies, still present significant challenges in the high-frequency regimes.

3.2 Ewald summation method ($d_\Lambda = 1, 2$)

The Ewald summation method was originally introduced [20] as a technique for evaluation of the electrostatic potential energy in crystals; its derivation in the context of the Helmholtz equation and, generally, wave-propagation phenomena is quite intricate, but a detailed description can be found in [27]. The representations that result after the application of this procedure expresses G_κ^q as a sum of two infinite series G_Λ^q and $G_{\Lambda^*}^q$,

$$G_\kappa^q = G_\Lambda^q + G_{\Lambda^*}^q, \tag{47}$$

indexed by elements in the lattices Λ and Λ^*, whose general terms decay as $\exp(-\eta^2 |\boldsymbol{R_n}|^2)$ and $\exp(-|\boldsymbol{K_n}|^2/4\eta^2)$ respectively. As indicated in [27], the "splitting parameter" $\eta > 0$ should be carefully chosen in order to maximize the convergence rate of the two series as well as to ensure the stability of the method (see [25, 32, 48]).

In what follows we present explicit expressions (whose derivation of can be found in [27]) for G_Λ^q and $G_{\Lambda^*}^q$ for various values of d and d_Λ. To present these expressions we let $\rho_{\boldsymbol{n}}$ denote the Euclidean distance between an observation point $\boldsymbol{x}$ and a lattice point $\boldsymbol{R_n}$, and we call $E_j = E_j(z)$ the exponential integral with complex argument z:

$$E_j(z) = \int_z^{\infty} \frac{\mathrm{e}^{-t}}{t^j} dt. \tag{48}$$

Then, for $d = 2$ and $d_\Lambda \leq d$, G^q_Λ is given by

$$G^q_\Lambda(\boldsymbol{x}) = \frac{1}{4\pi} \sum_{\boldsymbol{m}\in\mathbb{Z}^{d_\Lambda}} \mathrm{e}^{\mathrm{i}\boldsymbol{\alpha}\cdot\boldsymbol{R}_{\boldsymbol{m}}} \sum_{j=0}^{\infty} \frac{1}{j!} \left(\frac{\kappa}{2\eta}\right)^{2j} E_{j+1}\left(\eta^2\rho^2_{\boldsymbol{m}}\right), \tag{49}$$

while for $d = 3$ and $d_\Lambda \leq d$,

$$G^q_\Lambda(\boldsymbol{x}) = \frac{1}{8\pi} \sum_{\boldsymbol{m}\in\mathbb{Z}^{d_\Lambda}} \frac{\mathrm{e}^{\mathrm{i}\boldsymbol{\alpha}\cdot\boldsymbol{R}_{\boldsymbol{m}}}}{\rho_{\boldsymbol{m}}} \left[\mathrm{e}^{\mathrm{i}k\rho_{\boldsymbol{m}}}\mathrm{erfc}\left(\eta\rho_{\boldsymbol{m}} + \mathrm{i}\frac{\kappa}{2\eta}\right) + \mathrm{e}^{-\mathrm{i}k\rho_{\boldsymbol{m}}}\mathrm{erfc}\left(\eta\rho_{\boldsymbol{m}} - \mathrm{i}\frac{\kappa}{2\eta}\right)\right]. \tag{50}$$

The corresponding expressions for $G^q_{\Lambda^*}$ are as follows. For $d = 2, 3$ and $d_\Lambda = d - 1$ $G^q_{\Lambda^*}$ is given by

$$G^q_{\Lambda^*}(\boldsymbol{x}) = \frac{\mathrm{i}}{4\mathcal{A}} \sum_{\boldsymbol{m}\in\mathbb{Z}^{d_\Lambda}} \frac{\mathrm{e}^{\mathrm{i}\boldsymbol{\alpha}_{\boldsymbol{m}}\cdot\boldsymbol{x}}}{\beta_{\boldsymbol{m}}} \left[\mathrm{e}^{\mathrm{i}\beta_{\boldsymbol{m}}x_d}\mathrm{erfc}\left(-\eta x_d - \mathrm{i}\frac{\beta_{\boldsymbol{m}}}{2\eta}\right) + \mathrm{e}^{-\mathrm{i}\beta_{\boldsymbol{m}}x_d}\mathrm{erfc}\left(\eta x_d - \mathrm{i}\frac{\beta_{\boldsymbol{m}}}{2\eta}\right)\right]. \tag{51}$$

while for $d = 3$ and $d_\Lambda = d - 2 = 1$

$$G^q_{\Lambda^*}(\boldsymbol{x}) = \frac{1}{4\pi\mathcal{A}} \sum_{\boldsymbol{m}\in\mathbb{Z}^{d_\Lambda}} \mathrm{e}^{i\boldsymbol{\alpha}_{\boldsymbol{m}}\cdot\boldsymbol{x}} \sum_{j=0}^{\infty} \frac{1}{j!} \left(\mathrm{i}\eta\sqrt{x_2^2 + x_3^2}\right)^{2j} E_{j+1}\left(-\frac{\beta^2_{\boldsymbol{m}}}{4\eta^2}\right). \tag{52}$$

3.3 Shifted Green function ($d_\Lambda = 1, 2$)

The conditionally convergent sum (27) owes its poor convergence rate to the slow decay of the free-space Green function at infinity. As detailed in [3] and [10], a certain half-space shifted Green function can be used to produce quasi-periodic Green functions with a user-prescribed algebraic decay—convergent at any configuration, including RW-anomalies. In brief, given a shift-parameter $h > 0$ and a unit-vector $\hat{\boldsymbol{v}}$, the half-space shifted Green function of order $j \geq 0$ is given by

$$G_{\kappa,j}(\boldsymbol{x}) = \sum_{\ell=0}^{j} (-1)^\ell \binom{j}{\ell} G_\kappa(\boldsymbol{x} + \ell h\hat{\boldsymbol{v}}), \tag{53}$$

where $\hat{\boldsymbol{v}}$ is a unit-vector orthogonal to the d_Λ-dimensional subspace that contains the lattice Λ and, for $d_\Lambda = 1$, is oriented outward radially from the lattice Λ. It can be shown that [3, 10] given $M > 0$, there exists a constant $C(h, M)$ such that for $|\boldsymbol{x}\cdot\hat{\boldsymbol{v}}| \leq M$ we have

$$|G_{\kappa,j}(\boldsymbol{x})| \leq C(h, M)|\boldsymbol{x}^{\mathrm{orth}}|^{-(j+1)/2} \tag{54}$$

if j is an even positive integer and

$$|G_{\kappa,j}(\boldsymbol{x})| \leq C(h, M)|\boldsymbol{x}^{\mathrm{orth}}|^{-(j/2+1)} \tag{55}$$

if j is an odd positive integer. In these expressions $\boldsymbol{x}^{\mathrm{orth}}$ is the projection of the point $\boldsymbol{x}$ into the plane orthogonal to $\hat{\boldsymbol{v}}$. The shifted quasi-periodic Green function, in turn, is given by

$$G^q_{\kappa,j}(\boldsymbol{x}) = \sum_{\boldsymbol{m}\in\mathbb{Z}^{d_\Lambda}} \mathrm{e}^{\mathrm{i}\boldsymbol{\alpha}\cdot\boldsymbol{R}_{\boldsymbol{m}}} G_{\kappa,j}(\boldsymbol{x} - \boldsymbol{R}_{\boldsymbol{m}}). \tag{56}$$

It is clear from (53) that the classical quasi-periodic Green function can be expressed in terms of $G^q_{\kappa,j}$:

$$G^q_\kappa(\boldsymbol{x}) = G^q_{\kappa,j}(\boldsymbol{x}) - \sum_{\ell=1}^{j}(-1)^\ell \binom{j}{\ell} G^q(\boldsymbol{x} + \ell h\hat{\boldsymbol{v}}). \tag{57}$$

Replacing the quasi-periodic Green functions in the finite sum in equation (57) by their corresponding spectral representations (which can be done for all points $\mathbf{x}$ such that $\mathbf{x}^\perp \neq -\ell h\hat{\boldsymbol{v}}$, $\ell = 1, \ldots, j$), and provided $(\kappa, \boldsymbol{\alpha}, \Lambda)$ is not a RW-anomaly triple, it follows that, as proposed in [4, Eqs. 4.5, 4.6], we may write

$$G^q_\kappa(\boldsymbol{x}) = G^q_{\kappa,j}(\boldsymbol{x}) - \frac{\mathrm{i}}{4\mathcal{A}} \sum_{m\in\mathbb{Z}} \sum_{\ell=1}^{j}(-1)^\ell \binom{j}{\ell} \mathrm{e}^{\mathrm{i}\alpha_m x_1} H_0^{(1)}\left(\beta_m(\kappa)|\boldsymbol{x}^\perp + \ell h\hat{\boldsymbol{v}}|\right) \tag{58}$$

if $d_\lambda = 1$, $d = 3$ and

$$G^q_\kappa(\boldsymbol{x}) = G^q_{\kappa,j}(\boldsymbol{x}) - \frac{\mathrm{i}}{2\mathcal{A}} \sum_{\boldsymbol{m}\in\mathbb{Z}^{d_\lambda}} \sum_{\ell=1}^{j}(-1)^\ell \binom{j}{\ell} \frac{\mathrm{e}^{\mathrm{i}\boldsymbol{\alpha}_{\boldsymbol{m}}\cdot\boldsymbol{x} + \mathrm{i}\beta_{\boldsymbol{m}}|x_d + \ell h|}}{\beta_{\boldsymbol{m}}} \tag{59}$$

if $d_\lambda = d - 1$. Equations (58) and (59), which are only valid for non-anomalous configurations, express the quasi-periodic Green function G^q_κ as a sum of two quantities, the first one contains the spatial singularities ($\boldsymbol{x} \in \Lambda$), while the second one contains the singular terms which arise as an RW-anomaly is approached. Equations (58) and (59) thus yield rapidly-convergent jointly spatial-spectral representations of G^q_κ that exhibit explicitly all spatial and spectral singular terms. On the basis of (59), reference [4] introduced the use of the Woodbury-Sherman-Morrison formulae as a means to overcome the difficulties around RW-anomalies for problems of scattering by arrays of particles in two dimensional space. The present contribution extends that work to enable applicability of the overall methodology to arbitrary periodic domains—by utilizing either the shifted Green function in the form (57) or, alternatively, either a modified version of the Laplace-type integral representation (33) (for $d_\Lambda = 1$, $d = 2, 3$) or, finally, a modified version of the Ewald-summation expression (47). The proposed extensions for all three cases are described in the following section.

4 Woodbury-Sherman-Morrison (WSM) regularization formalism

4.1 BIE formulations

For simplicity, in this contribution attention is restricted to integral solvers for scalar Helmholtz problems in periodic structures with smooth boundaries, but any integral equation methodology (with application to e.g. open and/or non-smooth surfaces, Maxwell or Elasticity equations, etc.) can be used in conjunction with any of the quasi-periodic Green function methods presented in this paper. All of the examples considered in the present contribution originate from representations of the scattered field u^{s} in terms of the single- and double-layer potentials

$$\mathcal{S}^q_\kappa[\psi](\boldsymbol{x}) = \int_{\gamma^\sharp} G^q_\kappa(\boldsymbol{x} - \boldsymbol{y})\psi(\boldsymbol{y})dS(\boldsymbol{y}) \quad \text{and} \quad \mathcal{D}^q_\kappa[\phi](\boldsymbol{x}) = \int_{\gamma^\sharp} \frac{\partial G^q_\kappa}{\partial\nu(\boldsymbol{y})}(\boldsymbol{x} - \boldsymbol{y})\phi(\boldsymbol{y})dS(\boldsymbol{y}), \tag{60}$$

for a Λ-periodic surface γ (see Remark 1) which equals either $\Gamma_{j\ell}$ for some $j < \ell$, or relevant portions of $\Gamma^{\rm imp}_{\mathcal{D}}$, or $\Gamma^{\rm imp}_{\mathcal{N}}$, respectively. (For example, the integral that represents the field in the domain Ω_0 in Figure 1 (left) includes single- and double-layer operators defined on the upper (circular) portions of $\Gamma^{\rm imp}$, but it does not include integrals over the component of $\Gamma^{\rm imp}$ closer to the bottom of the figure.)

As is known, both potentials in (60) are solutions of the Helmholtz equation with wavenumber κ for $\boldsymbol{x} \notin \gamma$. We thus assume that the unknown scattered field has been expressed in terms of a boundary integral representation of the form

$$u^{\rm s}(\boldsymbol{x}) = \mathcal{T}[\boldsymbol{\Phi}](\boldsymbol{x}) \tag{61}$$

where

$$\mathcal{T}[\boldsymbol{\Phi}](\boldsymbol{x}) = \mathcal{T}_j[\boldsymbol{\Phi}](\boldsymbol{x}) \quad \text{for} \quad \boldsymbol{x} \in \Omega_j, \tag{62}$$

with $\mathcal{T}_j[\boldsymbol{\Phi}](\boldsymbol{x})$ given, for $\boldsymbol{x} \in \Omega_j$, by linear combinations of integral expressions of the form (60) involving Green functions corresponding to the domain Ω_j, as suggested above, and as illustrated further below in this section, and where $\boldsymbol{\Phi}$ is either a scalar density, or a vector containing such densities. This procedure reduces the scattering problem under consideration to a system of integral equations of the form

$$(J + T)[\boldsymbol{\Phi}] = \boldsymbol{F} \tag{63}$$

over appropriately chosen Banach spaces X of functions (that are typically selected as Sobolev spaces [37] or Hölder spaces [15]), where $T : X \to X$ is a compact operator, and where J either vanishes (in first-kind Fredholm equations) or is an invertible bounded operator (in second-kind Fredholm equations).

Thus, for example, in the case of an impenetrable scattering structure for which $\Omega = \Omega_0$ is a volume having as boundary a periodic surface $\Gamma^{\rm imp}$, the fields $u^s = \mathcal{S}^q_{n_0k}[\varphi]$ and $u^s = \mathcal{D}^q_{n_0k}[\varphi]$ with $\gamma = \Gamma^{\rm imp}$ are solutions of the sound-hard or sound-soft scattering problems respectively, with boundary conditions given in (13), provided the density φ satisfies the corresponding boundary integral equations

$$-\frac{1}{2}\varphi(\boldsymbol{x}) + \int\limits_{(\Gamma^{\rm imp})^\sharp} \frac{\partial G^q_\kappa}{\partial \nu(\boldsymbol{x})}(\boldsymbol{x}-\boldsymbol{y})\varphi(\boldsymbol{y})dS(\boldsymbol{y}) = -\frac{\partial u^{\rm inc}}{\partial \nu(\boldsymbol{x})}, \quad x \in (\Gamma^{\rm imp})^\sharp, \quad \text{or} \tag{64}$$

$$\frac{1}{2}\varphi(\boldsymbol{x}) + \int\limits_{(\Gamma^{\rm imp})^\sharp} \frac{\partial G^q_\kappa}{\partial \nu(\boldsymbol{y})}(\boldsymbol{x}-\boldsymbol{y})\varphi(\boldsymbol{y})dS(\boldsymbol{y}) = -u^{\rm inc}(\boldsymbol{x}), \quad x \in (\Gamma^{\rm imp})^\sharp. \tag{65}$$

In cases in which periodic arrays of impenetrable scattering particles are included, combined-field formulations are necessary to eliminate internal resonances [15]. In these two cases, the boundary potential $\mathcal{T}$ in equation (61) is either $\mathcal{S}^q_{n_0k}$ or $\mathcal{D}^q_{n_0k}$ whereas J in equation (63) are minus or plus a half of the identity operator of the underlying space X and T is either the normal derivative of the single layer potential or the values of the double layer potential at the surface $(\Gamma^{\rm imp})^\sharp$.

In addition to the impenetrable cases mentioned above, a specially well studied case concerns situations in which the refractive index $n(\boldsymbol{x})$ assumes only two values, n_0 and n_1 and the impenetrable region is empty (i.e., $\Omega = \mathbb{R}^d$). In such cases the scattered field admits the representation

$$u^{\rm s}(\boldsymbol{x}) = \begin{cases} \mathcal{D}^q_{n_0k}\left[\varphi - u^{\rm inc}\right](\boldsymbol{x}) - \mathcal{S}^q_{n_0k}\left[\frac{1}{C_{01}^2}\psi - \frac{\partial u^{\rm inc}}{\partial \nu}\right](\boldsymbol{x}), & \boldsymbol{x} \in \Omega_0 \\ -\mathcal{D}^q_{n_1k}\left[\varphi\right](\boldsymbol{x}) + \mathcal{S}^q_{n_1k}\left[\psi\right](\boldsymbol{x}), & \boldsymbol{x} \in \Omega_1 \end{cases} \tag{66}$$

in terms of single- and double-layer potentials, where the densities φ and ψ satisfy the system of integral equations

$$\left(\begin{bmatrix} \mathrm{Id} & 0 \\ 0 & \frac{1+C_{01}^{-2}}{2}\mathrm{Id} \end{bmatrix} - \begin{bmatrix} D_0^q - D_1^q & -(C_{01}^{-2}S_0^q - S_1^q) \\ N_0^q - N_1^q & -(C_{01}^{-2}K_0^q - K_1^q) \end{bmatrix}\right)\begin{bmatrix} \varphi \\ \psi \end{bmatrix} = \begin{bmatrix} u^{\mathrm{inc}} \\ \frac{\partial u^{\mathrm{inc}}}{\partial \nu} \end{bmatrix}, \quad \boldsymbol{x} \in \Gamma_{01}^\sharp. \tag{67}$$

Here the operators S_j^q, D_j^q are defined as the restriction to the boundary curve $\gamma^\sharp$ of the single- and double-layer potentials (60) with $\gamma = \Gamma_{01}$ and $\kappa = n_j k$ ($j = 0, 1$). The operator N_j^q and K_j^q, in turn, denote the normal derivative on $\gamma^\sharp$ of the double-layer potential and the adjoint of D_j^q (in the sense of [15], i.e., without complex conjugation), respectively, once again, using $\kappa = n_j k$. A comprehensive discussion of the properties and character of these operators can be found in [15]. Clearly, in the present case $\mathcal{T}$ in equation (61) can be identified with the right-hand side of (66), and the quantities and J and T in equation (63) equal the first and second square-bracketed terms in (67).

Remark 3. For configurations containing a periodic array of penetrable particles (e.g. Ω_2 in Figure 1 left), the representation formula (66) can be advantageously modified by utilizing the corresponding free-space Green function, instead of the quasi-periodic Green function, to represent fields in the interior of the particles. The integral equations (67) need to be modified accordingly. Use of this strategy, which clearly eliminates the cost of the evaluation of the quasi-periodic Green function for all integral operators corresponding to the interior of the particles, was utilized in this paper in all relevant cases.

As in the three prototypical cases embodied by equations (64) through (67), for general periodic structures of the type described in Section 2, the operator T in equation (63) equals a combination of integral operators over the unit cell $\left(\Gamma_s^{\mathrm{imp}}\right)^\sharp$, $\left(\Gamma_h^{\mathrm{imp}}\right)^\sharp$ and $(\Gamma_{j\ell})^\sharp$ ($1 \le j < \ell \le r+1$) of the various scattering surfaces. Each one of these operators utilizes either a quasi-periodic or a free-space Green function with an appropriate value of the wavenumber κ, or a combination of quasi-periodic Green functions for two different wavenumbers. Clearly, these integral equation systems are only meaningful provided no Wood anomalies arise in the overall scattering setup. The regularization methodology we propose, which yields integral equation formulations that are valid throughout the spectrum, including RW anomalies, is described in the following section.

4.2 A well-conditioned system throughout the spectrum: WSM regularization

This section shows that the system of integral equations (63) is ill-conditioned around RW-anomalies, and it proposes a regularization technique, the WSM method, which yields a reformulation of this system of equations which does not break down as anomalous configurations are either approached or reached. To do this, in what follows, given a fixed triple $(k, \boldsymbol{\alpha}, \Lambda)$, which we call a *primitive* triple, we associate to each domain Ω_j a corresponding *derived* triple $(n_j k, \boldsymbol{\alpha}, \Lambda)$. Letting $(k_w, \boldsymbol{\alpha}_w, \Lambda_w)$ denote a primitive triple for which, for at least one value of j , the corresponding j-th domain derived triple $(n_j k_w, \boldsymbol{\alpha}_w, \Lambda_w)$ is a RW-anomaly, for a given primitive triple $(k, \boldsymbol{\alpha}, \Lambda)$ in the vicinity of $(k_w, \boldsymbol{\alpha}_w, \Lambda_w)$, the Green function expressions (29) and (30) for the wavenumber $n_j k$ can be re-expressed in the regular/singular form

$$G_{n_j k}^q(\boldsymbol{x}) = G_{n_j k}^{\mathrm{reg}}(\boldsymbol{x}) + C(d, d_\Lambda) \sum_{\boldsymbol{m} \in \mathcal{W}_j} \mathrm{e}^{i\boldsymbol{\alpha}_{\boldsymbol{m}} \cdot \boldsymbol{x}} f(\beta_{\boldsymbol{m}}(n_j k)) \tag{68}$$

where the regular part $G^{\mathrm{reg}}_{n_jk}$ is well defined for $(k,\boldsymbol{\alpha},\Lambda)$ equal to and in a vicinity of $(k_w,\boldsymbol{\alpha}_w,\Lambda_w)$, and where the second term on the right-hand side contains the singularity that arises as the RW anomaly is approached. In (68) the function $f(t)$ is given by $f(t)=1/t$ for $d_\Lambda=d-1$, $d=2,3$, and $f(t)=2\mathrm{i}/\pi\log(t/2)$ for $d_\Lambda=1$, $d=3$; the constant $C(d,d_\Lambda)$ equals the pre-factor that multiplies the infinite sums in equations (29)–(30); and $\mathcal{W}_j=\mathcal{W}(n_jk_w,\boldsymbol{\alpha}_w,\Lambda_w)$ (see equation (32)). The derivation of (68) results easily from simple manipulations including use of the relations

$$\frac{\mathrm{e}^{\mathrm{i}t}}{t}-\frac{1}{t}\to\mathrm{i}\quad\text{and}\quad H_0^{(1)}(t)-\frac{2\mathrm{i}}{\pi}\log\left(\frac{t}{2}\right)\to\frac{2\mathrm{i}}{\pi}C\quad\text{as}\quad t\to 0, \tag{69}$$

where C denotes the Euler-Mascheroni constant, $C=0.5772156649....$

Letting T_{reg} and T_{W} denote the (possibly matrix-valued) integral operators that are obtained by replacing the quasi-periodic Green function(s) $G^q_{n_jk}(\boldsymbol{x}-\boldsymbol{y})$ (for which the derived triple $(n_jk,\boldsymbol{\alpha},\Lambda)$ is close to an RW-anomaly) and their normal derivatives in the definition of the operator T by the expressions arising from the first and last terms on the right-hand side of equation (68), respectively, equation (63) may be re-expressed in the form

$$(A+T_W)\boldsymbol{\Phi}=\boldsymbol{F},\quad\text{where}\quad A=J+T_{\mathrm{reg}}. \tag{70}$$

The operator T_{W}, in turn, may be expressed in the form

$$T_{\mathrm{W}}=E_{\mathrm{W}}D^{-1}R_{\mathrm{W}}, \tag{71}$$

where R_{W} denotes the finite rank integral operator resulting from replacement of $G^q_{n_jk}$ in the definition of T by the kernel

$$\sum_{\boldsymbol{m}\in\mathcal{W}_j}\mathrm{e}^{\mathrm{i}\boldsymbol{\alpha}_{\boldsymbol{m}}\cdot(\boldsymbol{x}-\boldsymbol{y})}; \tag{72}$$

where, letting X_{W} denote the (finite-dimensional) image (spanned by a certain finite basis $\{\Phi_{\boldsymbol{m}}:\boldsymbol{m}\in\bigcup_j\mathcal{W}_j\}$) of R_{W}, $D:X_{\mathrm{W}}\to X_{\mathrm{W}}$ is defined over the basis elements $\Phi_{\boldsymbol{m}}$ as

$$D\,\Phi_{\boldsymbol{m}}=\frac{1}{f(\beta_{\boldsymbol{m}}(n_jk))}\Phi_{\boldsymbol{m}},\quad\boldsymbol{m}\in\mathcal{W}_j \tag{73}$$

(and subsequently extended by linearity), and where E_{W} is the inclusion operator of X_{W} into X.

The definitions of the finite-dimensional space X_{W}, its basis $\{\Phi_{\boldsymbol{m}}:\boldsymbol{m}\in\bigcup_j\mathcal{W}_j\}$, and the operator D become apparent as the replacement of the corresponding $G^q_{n_jk}$ by the separable kernel (72) is effected. For instance, in the examples considered in Section 4.1 we have

$$\Phi_{\boldsymbol{m}}(\boldsymbol{x})=\partial_{\nu(\boldsymbol{x})}\left(e^{\mathrm{i}\boldsymbol{\alpha}_{\boldsymbol{m}}\cdot\boldsymbol{x}}\right),\quad\boldsymbol{x}\in\partial\Omega^\sharp,\quad\boldsymbol{m}\in\mathcal{W}_0 \tag{74}$$

for equation (64),

$$\Phi_{\boldsymbol{m}}(\boldsymbol{x})=e^{\mathrm{i}\boldsymbol{\alpha}_{\boldsymbol{m}}\cdot\boldsymbol{x}},\quad\boldsymbol{x}\in\partial\Omega^\sharp,\quad\boldsymbol{m}\in\mathcal{W}_0 \tag{75}$$

for equation (65) and

$$\Phi_{\boldsymbol{m}}(\boldsymbol{x})=\begin{bmatrix}e^{\mathrm{i}\boldsymbol{\alpha}_{\boldsymbol{m}}\cdot\boldsymbol{x}}\\ \partial_{\nu(\boldsymbol{x})}\left(e^{\mathrm{i}\boldsymbol{\alpha}_{\boldsymbol{m}}\cdot\boldsymbol{x}}\right)\end{bmatrix},\quad\boldsymbol{x}\in\Gamma_{01},\quad\boldsymbol{m}\in\mathcal{W}_j \tag{76}$$

for equation (67). In the first two cases, the finite-rank operator R_W assumes the same form, namely

$$R_W[\varphi](\boldsymbol{x}) = C(d, d_\Lambda) \sum_{\boldsymbol{m}\in\mathcal{W}_0} I_{\boldsymbol{m}}[\varphi]\Phi_{\boldsymbol{m}}, \tag{77}$$

but the corresponding functionals $I_{\boldsymbol{m}}$ for equations (64) and (65) are given by

$$I_{\boldsymbol{m}}[\varphi] = \int\limits_{(\Gamma^{\rm imp})^\sharp} e^{-{\rm i}\boldsymbol{\alpha}_{\boldsymbol{m}}\cdot\boldsymbol{y}}\varphi(\boldsymbol{y})dS(\boldsymbol{y}) \quad \text{and} \quad I_{\boldsymbol{m}}[\varphi] = \int\limits_{(\Gamma^{\rm imp})^\sharp} \partial_{\nu(\boldsymbol{x})}\left(e^{-{\rm i}\boldsymbol{\alpha}_{\boldsymbol{m}}\cdot\boldsymbol{y}}\right)\varphi(\boldsymbol{y})dS(\boldsymbol{y}), \tag{78}$$

respectively. In the case of the transmission problem (equation (67)), in turn, we have

$$R_W[\boldsymbol{\Phi}](\boldsymbol{x}) = C(d, d_\Lambda)\left(\sum_{\boldsymbol{m}\in\mathcal{W}_0} I_{\boldsymbol{m}}[\Phi]\Phi_{\boldsymbol{m}} - \sum_{\boldsymbol{m}\in\mathcal{W}_1} J_{\boldsymbol{m}}[\Phi]\Phi_{\boldsymbol{m}}\right) \tag{79}$$

with $\boldsymbol{\Phi} = \begin{bmatrix}\varphi\\ \psi\end{bmatrix}$, where we have set

$$I_{\boldsymbol{m}}[\boldsymbol{\Phi}] = \int\limits_{(\Gamma_{01})^\sharp} \left[\partial_{\nu(\boldsymbol{y})}\left(e^{-{\rm i}\boldsymbol{\alpha}_{\boldsymbol{m}}\cdot\boldsymbol{y}}\right)\varphi(\boldsymbol{y}) - e^{-{\rm i}\boldsymbol{\alpha}_{\boldsymbol{m}}\cdot\boldsymbol{y}}\psi(\boldsymbol{y})\right]dS(\boldsymbol{y}) \quad \text{and} \tag{80}$$

$$J_{\boldsymbol{m}}[\boldsymbol{\Phi}] = \int\limits_{(\Gamma_{01})^\sharp} \left[\partial_{\nu(\boldsymbol{y})}\left(e^{-{\rm i}\boldsymbol{\alpha}_{\boldsymbol{m}}\cdot\boldsymbol{y}}\right)\varphi(\boldsymbol{y}) - \frac{1}{C_{01}^2}e^{-{\rm i}\boldsymbol{\alpha}_{\boldsymbol{m}}\cdot\boldsymbol{y}}\psi(\boldsymbol{y})\right]dS(\boldsymbol{y}). \tag{81}$$

Substitution of (71) in (70) shows that the original integral equation (63) can be expressed in the form

$$(A + E_{\rm W}D^{-1}R_{\rm W})\boldsymbol{\Phi} = \boldsymbol{F}. \tag{82}$$

The inverse of the operator on the left-hand side can be obtained on the basis of the Woodbury formula

$$(A + E_{\rm W}D^{-1}R_{\rm W})^{-1} = A^{-1} - A^{-1}E_{\rm W}(D + R_{\rm W}A^{-1}E_{\rm W})^{-1}R_{\rm W}A^{-1} \tag{83}$$

(see (Remark 4)) provided the operators A and $(D + R_{\rm W}A^{-1}E_{\rm W})$ are invertible.

Equation (83) is a crucial element of our treatment of the RW-anomaly problem. Assuming that the operator A is invertible and well-conditioned:

1. It expresses the inverse operator on the left-hand side in terms of the inverse of the operator A—that only involves the quantities $G^{\rm reg}_{n_jk}$ (as defined in (68)), which are well-defined at and around RW-anomalies;

2. It encapsulates the ill-conditioning of (82) at RW-anomalies through the explicit diagonal operator D^{-1} (which blows up as the anomaly is reached) but which only manifests itself on the right hand side of (83), through its inverse D (which tends to zero as the anomalous configuration is approached); and,

3. Its right-hand expression shows that the inverse operator on the left-hand side of that equation actually has a removable singularity at the RW anomaly under consideration, and it provides a useful formula for solution of equation (63) at and around $(k_w, \boldsymbol{\alpha}_w, \Lambda_w)$.

The Woodbury formula (83) additionally requires the inversion of the operator $D+T_{\mathrm{W}}A^{-1}E_{\mathrm{W}}$. But this inversion problem can easily be translated into a finite-dimensional matrix inversion problem—since this operator is defined over the finite-dimensional space X_W. A numerical study of the conditioning of the WSM-regularized operators, which is is presented in Section 5, demonstrate the value of the WSM framework.

Remark 4. The Woodbury formula is usually introduced in the context of fast-inversion of matrices; it commonly reads [44]

$$(A+UCV)^{-1} = A^{-1} - A^{-1}U(C^{-1}+VA^{-1}U)^{-1}VA^{-1} \tag{84}$$

where $A \in \mathbb{C}^{n\times n}$, $U \in \mathbb{C}^{n\times k}$, $C \in \mathbb{C}^{k\times k}$ and $V \in \mathbb{C}^{k\times n}$ with k usually much smaller than n (the case $k=1$ is also known as the Sherman-Morrison formula.) But, as equation (84) can be established by mere substitution and algebraic manipulation, the formula is valid for infinite-dimensional operators as well. Briefly, equation (84) holds for arbitrary operators provided 1) the operator A is invertible, 2) the domains and ranges of the operators U, C and V are such that the composition UCV is well-defined, 3) the operator C is invertible in the space in which it is defined, and, 4) the operator $C^{-1}+VA^{-1}U$ is invertible.

4.3 Evaluation of scattering solutions at and around RW-anomalies

Once the underlying operator equation is solved, the values of the solution of the PDE problem under consideration are obtained via evaluation of the boundary potential (61) using as surface density the solution $\mathbf{\Phi}$ of the integral equation. As mentioned at the beginning of Section 4.1, all solutions of the Helmholtz equation considered in this paper utilize the quasi-periodic Green function (27) with various wavenumbers, and their normal derivatives, as kernels of the single and double layer potentials. However, this particular Green function ceases to exist at RW-anomalies and therefore, as shown in what follows, an additional step is needed to produce the desired quasi-periodic solutions of the Helmholtz equation for anomalous configurations.

To do this we first use equation (68) to produce a decomposition of the potentials in (61) into a regular and a singular part,

$$\mathcal{T}_{\mathrm{reg}}\left[\mathbf{\Phi}\right] = \mathcal{T}_{\mathrm{reg}}\left[\mathbf{\Phi}\right] + \mathcal{T}_{\mathrm{W}}\left[\mathbf{\Phi}\right], \tag{85}$$

analogous to the decomposition introduced previously for the operator T. For example, in the impenetrable case with either sound-hard or sound-soft boundary conditions, the scattered field is given by a single layer potential or a double layer potential, respectively (see equations (64) and (65)). After replacement of the quasi-periodic Green function by (68) we obtain the representation

$$u^{\mathrm{s}}(\boldsymbol{x}) = \int_{(\Gamma^{\mathrm{imp}})^\sharp} G^{\mathrm{reg}}_{n_0k}(\boldsymbol{x}-\boldsymbol{y})\varphi(\boldsymbol{y})dS(\boldsymbol{y}) + C(d,d_\Lambda)\sum_{\boldsymbol{m}\in\mathcal{W}_0} e^{\mathrm{i}\boldsymbol{\alpha}_{\boldsymbol{m}}\cdot\boldsymbol{x}} f\left(\beta_{\boldsymbol{m}}(n_0k)\right) I_{\boldsymbol{m}}[\varphi], \quad \boldsymbol{x}\in\Omega_0 \tag{86}$$

for the single layer case and

$$u^{\mathrm{s}}(\boldsymbol{x}) = \int_{(\Gamma^{\mathrm{imp}})^\sharp} \frac{\partial G^{\mathrm{reg}}_{n_0k}}{\partial\nu(\boldsymbol{y})}(\boldsymbol{x}-\boldsymbol{y})\varphi(\boldsymbol{y})dS(\boldsymbol{y}) + C(d,d_\Lambda)\sum_{\boldsymbol{m}\in\mathcal{W}_0} e^{\mathrm{i}\boldsymbol{\alpha}_{\boldsymbol{m}}\cdot\boldsymbol{x}} f\left(\beta_{\boldsymbol{m}}(n_0k)\right) I_{\boldsymbol{m}}[\varphi]. \quad \boldsymbol{x}\in\Omega_0 \tag{87}$$

for the double layer case, where the functionals $I_{\boldsymbol{m}}$ are given by equation (78). For the transmission case, in turn, the scattered field is a linear combination of single and double layer potentials (see

equation (66)) and after replacement of the quasi-periodic Green functions by (68) we obtain

$$u^{\mathrm{s}}(\boldsymbol{x}) = \int\limits_{\Gamma_{01}^{\sharp}} \frac{\partial G_{n_0k}^{\mathrm{reg}}}{\partial \nu(\boldsymbol{y})}(\boldsymbol{x}-\boldsymbol{y})\varphi(\boldsymbol{y})dS(\boldsymbol{y}) - \frac{1}{C_{01}^2}\int\limits_{\Gamma_{01}^{\sharp}} G_{n_0k}^{\mathrm{reg}}(\boldsymbol{x}-\boldsymbol{y})\psi(\boldsymbol{y})dS(\boldsymbol{y}) + C(d,d_\Lambda)\sum_{\boldsymbol{m}\in\mathcal{W}_0} e^{\mathrm{i}\boldsymbol{\alpha}_{\boldsymbol{m}}\cdot\boldsymbol{x}} f\left(\beta_{\boldsymbol{m}}(n_0k)\right) J_{\boldsymbol{m}}[\varphi], \quad \boldsymbol{x}\in\Omega_0, \tag{88}$$

$$u^{\mathrm{s}}(\boldsymbol{x}) = -\int\limits_{\Gamma_{01}^{\sharp}} \frac{\partial G_{n_1k}^{\mathrm{reg}}}{\partial \nu(\boldsymbol{y})}(\boldsymbol{x}-\boldsymbol{y})\varphi(\boldsymbol{y})dS(\boldsymbol{y}) + \int\limits_{\Gamma_{01}^{\sharp}} G_{n_1k}^{\mathrm{reg}}(\boldsymbol{x}-\boldsymbol{y})\psi(\boldsymbol{y})dS(\boldsymbol{y}) - C(d,d_\Lambda)\sum_{\boldsymbol{m}\in\mathcal{W}_1} e^{\mathrm{i}\boldsymbol{\alpha}_{\boldsymbol{m}}\cdot\boldsymbol{x}} f\left(\beta_{\boldsymbol{m}}(n_1k)\right) I_{\boldsymbol{m}}[\varphi], \quad \boldsymbol{x}\in\Omega_1. \tag{89}$$

where $I_{\boldsymbol{m}}$ and $J_{\boldsymbol{m}}$ are given by Equations (80) and (81). In these examples, either $f(\beta_{\boldsymbol{m}}(n_0k))$ or $f(\beta_{\boldsymbol{m}}(n_1k))$ (or both) diverges as the anomalous configuration is approached but, as shown in what follows, all the corresponding products of the diverging $f(\beta_{\boldsymbol{m}}(n_jk))$ by each of the possible functionals tend to a limit as the anomalous configuration is approached.

Indeed, in the general case (61) (and in particular in the examples considered in Section 4.1), these products are no other than the coordinates of the operator $D^{-1}R_W$ expressed in the corresponding basis $\{\Phi_{\boldsymbol{m}} : \boldsymbol{m}\in\mathcal{W}_j\}$. Thus, in order to evaluate the needed products at or around an RW anomaly, it suffices to compute the quantity $D^{-1}R_{\mathrm{W}}\boldsymbol{\Phi}$, where $\boldsymbol{\Phi}$ is the solution of (82) obtained by means of the Woodbury formula (83)—either at a near anomalous configuration, or in the limit as the anomaly is reached. To do this we consider the following sequence of relations:

$$\begin{aligned} D^{-1}R_{\mathrm{W}}\boldsymbol{\Phi} &= D^{-1}R_{\mathrm{W}}\left(A^{-1} - A^{-1}E_{\mathrm{W}}(D+R_{\mathrm{W}}A^{-1}E_{\mathrm{W}})^{-1}R_{\mathrm{W}}A^{-1}\right)\boldsymbol{F} \\ &= D^{-1}R_{\mathrm{W}}A^{-1}\boldsymbol{F} - D^{-1}R_{\mathrm{W}}A^{-1}E_{\mathrm{W}}(D+R_{\mathrm{W}}A^{-1}E_{\mathrm{W}})^{-1}R_{\mathrm{W}}A^{-1}\boldsymbol{F} \\ &= \left[D^{-1}\left(D+R_{\mathrm{W}}A^{-1}E_{\mathrm{W}}\right) - D^{-1}R_{\mathrm{W}}A^{-1}E_{\mathrm{W}}\right]\left(D+R_{\mathrm{W}}A^{-1}E_{\mathrm{W}}\right)^{-1}R_{\mathrm{W}}A^{-1}\boldsymbol{F} \\ &= \left(D+R_{\mathrm{W}}A^{-1}E_{\mathrm{W}}\right)^{-1}R_{\mathrm{W}}A^{-1}\boldsymbol{F}. \end{aligned} \tag{90}$$

The only slightly non-trivial step in this derivation, namely, the third equality, is established by factoring out the term $(D+R_{\mathrm{W}}A^{-1}E_{\mathrm{W}})^{-1}R_{\mathrm{W}}A^{-1}\boldsymbol{F}$ from the right. Note that, as in (83), the inverse of the sum on the last line in (90) can be obtained by solving a finite-dimensional linear system of equations. Since the last line in this equation tends to a finite limit as the RW configuration is approached, the coordinates of $D^{-1}R_{\mathrm{W}}\boldsymbol{\Phi}$ can be continuously extended in the RW-anomaly limit. Thus, the spatial values of the solution of the PDE under consideration can be continuously extended to the anomalous configuration $(k_w, \boldsymbol{\alpha}_{\boldsymbol{w}}, \Lambda_w)$ by means of the expression in the last line of (90).

5 Numerical results

This section presents results of a variety of numerical experiments that demonstrate the applicability and performance of the Laplace-type, Ewald and shifted Green function RW-capable methodologies proposed in this article for evaluation of scattering solutions both at and away from RW-anomalies. The two-dimensional scattering structures (Section 5.3) are arrays of penetrable and impenetrable particles, whereas in the more challenging bi-periodic three-dimensional case (Section 5.4) we also

consider arrays of impenetrable particles as well as bi-periodic reflective and transmissive gratings (see also Remark 3 in regard to penetrable particles). Finally, in the case $d_\Lambda = 1$, $d = 3$, the solvers are demonstrated with the simulation of acoustical wave-scattering by impenetrable double-helical periodic structures (Section 5.5).

The accurate evaluation of weakly-singular integrals arising in boundary integral equation methods is obtained by means of the well known Martensen-Kussmaul rule described in [16] in the case $d = 2$ whereas for $d = 3$ we use the novel "rectangular-integration" methodology introduced in [5]. All simulations were obtained by means of a Fortran-90 implementation of the numerical solvers and the various figures were rendered using the visualization software VisIt [13]. The two-dimensional simulations were executed in a single core of an Intel i5-8250U processor in a personal computer with 16 Gb of RAM memory. The solvers for the various three-dimensional examples were run in 24 cores of an Intel(R) Xeon(R) CPU E5-2670 v3 processor with 120 Gb of RAM memory; the code was parallelized using the OpenMP API. The linear systems in the two-dimensional case were solved by Gaussian elimination using the LAPACK implementation provided in the Intel Math Kernel Library; in the three dimensional examples, in turn, the solutions were obtained using the CERFACS implementation of the GMRES algorithm [21] (in these cases we have reported the number of iterations required to achieve a residual tolerance of 10^{-12} .) Throughout this section the overall solver errors are estimated by means of resolution studies as well as the energy balance criterion (EBC), that is, the defect in energy balance (a topic that is discussed in Appendix A).

Remark 5. The necessary parameters required for the various quasi-periodic Green function evaluation methods were selected as follows. The shift parameter and numbers of shifts used for the shifted Green function (which is employed in Sections 5.2 and 5.5) are $h = \lambda/2$ and $j = 8$. The splitting parameter in the Ewald method (which is employed in Sections 5.2, 5.3 and 5.4) was selected as $\eta = k$. The Laplace-type integral method (which is utilized in Section 5.2) only requires a selection of the number of quadrature points; a number of 128 quadrature points was used in all cases.

5.1 Accurate evaluation of the quasi-periodic Green function G^q_κ

Use of the Ewald method results in highly-efficient solvers [48], at least for configurations of sufficiently (acoustically) small period, as a result of the exponential decay of the general $\boldsymbol{m}$-term in both series in equation (47). For example, for acoustically-small bi-periodic configurations in three dimensions, evaluation of one value of the Green function by means of the Ewald method can be produced in a fraction of a millisecond with machine-precision accuracy. However, as demonstrated in [2, 12], the Ewald method becomes highly unstable as the frequency or the size of the period grows, rendering the methodology completely inaccurate at high frequencies; in our experiments we have found that for problems where the period equals 64 wavelengths the Ewald approach does not provide any accuracy for any possible choice of the splitting parameter η. As explained in Section 3, in turn, the Laplace-type integral technique can only be applied for cases in which $d_\Lambda = 1$ (with the exception of bi-periodic arrays for which the periodicity directions are orthogonal) and, in the most challenging three-dimensional, $d_\Lambda = 1$, case the evaluation of Bessel functions with complex argument that it requires makes the method much slower than the Ewald approach—requiring tens of milliseconds per evaluation to produce single-precision accuracy. (Moreover, since the argument of the Bessel function needed by the Laplace-type method is proportional to $\kappa|\boldsymbol{x}^\perp|$, instabilities arise in higher-frequency/period regimes, but this problem was resolved in [23, 24].)

Period ($d_\Lambda = 1$)	8	16	32	Computing time (s)
2.5λ	$4.2 \cdot 10^{-3}$	$7.2 \cdot 10^{-5}$	$1.2 \cdot 10^{-6}$	$\mathcal{O}(10^{-4})$
8.5λ	$2.9 \cdot 10^{-5}$	$3.6 \cdot 10^{-7}$	$5.3 \cdot 10^{-9}$	$\mathcal{O}(10^{-4})$
64.5λ	$2.2 \cdot 10^{-7}$	$1.3 \cdot 10^{-9}$	$1.5 \cdot 10^{-11}$	$\mathcal{O}(10^{-4})$

Period ($d_\Lambda = 2$)	2	4	8	Computing time (s)
2.5λ	$2.3 \cdot 10^{+2}$	$2.3 \cdot 10^{+2}$	$2.3 \cdot 10^{+2}$	$\mathcal{O}(10^{-4})$
8.5λ	$1.6 \cdot 10^{-1}$	$5.2 \cdot 10^{-3}$	$1.3 \cdot 10^{-7}$	$\mathcal{O}(10^{-3})$
64.5λ	$1.5 \cdot 10^{-11}$	$1.9 \cdot 10^{-11}$	$2.9 \cdot 10^{-11}$	$\mathcal{O}(10^{-2})$

Table 1: Errors and computing times (in seconds) required for single-point evaluation of the shifted Green-function expression (59) truncated with $N = 8, 16, 32$ (upper table) and $N = 2, 4, 8$ (lower table) in three-dimensional with periodicity $d_\Lambda = 1$ (top) and $d_\Lambda = 2$ (bottom). (For conciseness, only order-of-magnitude computing times, which are constant for each row, are reported.) The errors displayed were evaluated as the maxima of errors at several points within the period for which $|\boldsymbol{x}^\perp|$ equals half of the period (a selection that was made to ensure the spectral series converges rapidly and can thus be used to evaluate reference values). In both cases the algorithm parameters are $j = 8$ and $h = 0.25\lambda^{-1}$. The number of terms kept in the truncation of the reciprocal-lattice sum in (59) was taken to coincide with the number of terms used in the spectral-sum evaluation of reference values (fewer terms could be used, but the larger numbers of terms induce only a marginal additional computing cost in these cases). The large errors observed for the smaller periods can be reduced by increasing the value of N (and, thus, the computing cost) as needed.

The proposed shifted Green-function based approach, finally, is the simplest of the three methods described in this article as it does not require the evaluation of special functions: only finite truncations of the sums over the direct and the reciprocal lattices inherent in the two terms in (59) are required. The reciprocal lattice sum is truncated as indicated in the caption of Table 1. The sum over the direct lattice (and therefore, the complete procedure), in turn, inherits the algebraic decay (54)–(55) of the shifted Green function. Thus, truncating the required spatial sum (56) by including only the terms $\boldsymbol{m} \in \mathbb{Z}^{d_\Lambda}$ with coordinates between $-N$ and N in each one of the d_Λ dimensions, the value of N required to achieve a given accuracy may be either small or large depending on whether the period is large or small, respectively, compared to the wavelength, as demonstrated in Table 1. The slow convergence in the small-period case is specially problematic for bi-periodic arrays in three-dimensional space as the computation of the finite truncations have a quadratic cost, since the sum must be performed over two directions. But, as shown in [8], this problem may be eliminated by means of suitable integral-equation acceleration methods. Additionally, even for small periods, for arrays with a single direction of periodicity ($d_\Lambda = 1$) only a one-dimensional spatial sum needs to be evaluated in the shifted Green function approach, making it extremely fast, as illustrated in Table 5—which is specially important in the three dimensional case where the Ewald method is highly-unstable, and where the Laplace-type integral technique can be orders of magnitude slower than the shifted Green function method. Furthermore, as demonstrated in Table 1 and [3, 10], for a fixed number of terms, the shifted Green function achieves higher and higher accuracies as the period is increased. Or, equivalently, since the accuracy, which scales like $L^{-(\frac{j}{2}-1)}$ for j even (with a slightly different exponent expression for j odd), the number of terms needed for the shifted Green function to meet a given desired error tolerance decreases as the period

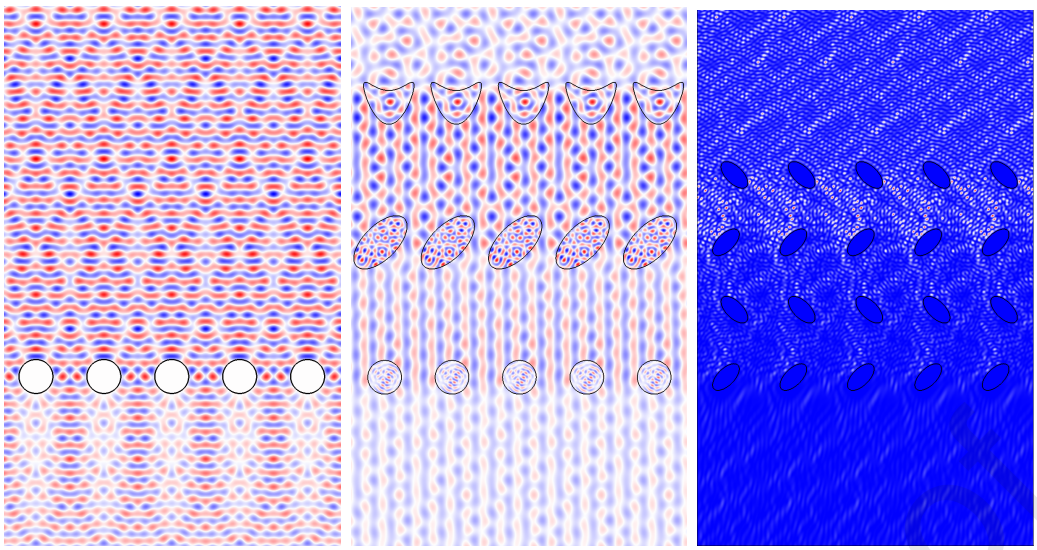

Figure 2: Real part of the total field observed under normal incidence by a periodic array of impenetrable sound-soft (left and right) and penetrable sound-hard (center) cylindrical obstacles with various cross-sections.

is increased. Since the computation of the quantities involved are not exponentially large or small, no instabilities as the ones in the Ewald or Laplace-type integral methods occur, making the shifted Green-function based method highly suitable for large-period configurations even in the case $d = 3$, $d_\Lambda = 2$.

In sum, our experiments show that in the cases $d_\Lambda = d - 1$ ($d = 2,\ 3$) the Ewald representation provides the best convergence properties for small periods but it becomes unstable at higher-frequencies. Additionally, the Ewald method is unstable at any frequency in the case $d_\lambda = 1$, $d = 3$. Fortunately, the shifted Green-function approach becomes computationally advantageous precisely in the high-frequency $d_\Lambda = d - 1$ ($d = 2,\ 3$) and $d_\lambda = 1$, $d = 3$ cases for which the Ewald method breaks down. Additionally, in view of the contribution [8], accelerated versions of the shifted Green function approach may prove competitive in low-frequency regimes as well. The Laplace-type method, in turn, is generally slower than the Ewald or shifted Green function methods in their respective preferred operation regimes. Therefore, except for a Laplace-method demonstration presented in Section 5.2, all of the numerical examples presented in this section utilize either the Ewald or shifted Green function methods, whichever is most efficient for each case studied.

5.2 Condition number analysis around RW-anomalies

Figure 2 (left) depicts the first scattering setup considered in this section, namely, a plane wave illuminating a two-dimensional periodic array, of period $L = 5\lambda$, of impenetrable sound-soft cylindrical obstacles. The individual sound-soft scatterers have circular cross-section with diameter equal to half a period, and the simulations carried out for this geometry contemplate angles close to normal incidence which, for the chosen period, is an RW anomalous configuration.

As stated in Section 1, the application of integral equation methods to periodic media normally present two main types of difficulties around RW-anomalies. The most dramatic challenge concerns inaccuracies in the evaluation of the quasi-periodic Green function—which result in an inaccurate

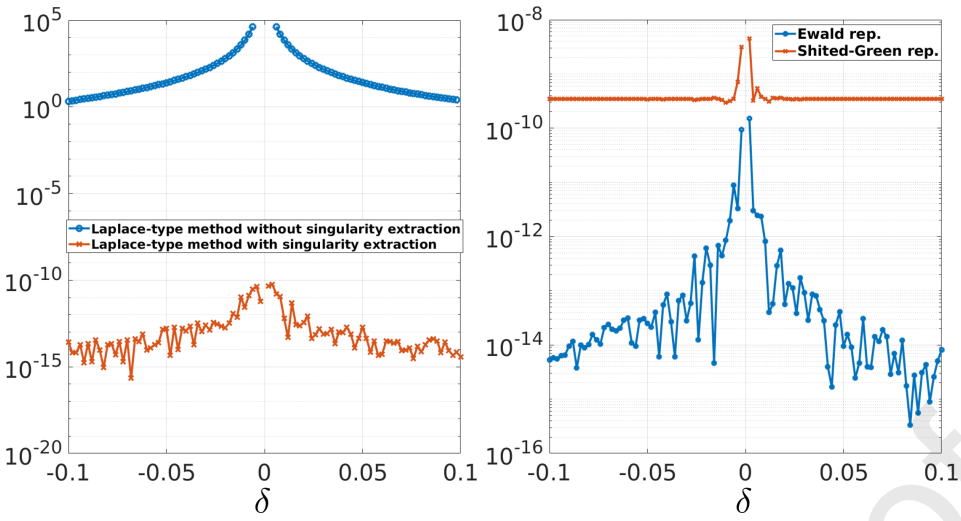

Figure 3: Left: errors, estimated by the energy balance criterion, as a function of $\delta = \theta^{\frac{1}{5}}$, for scattering solvers based on the Laplace integral method. The Laplace-type method demonstrated in the left graph, computes accurately or inaccurately, depending on whether singularity extraction is performed or not, the quasi-periodic Green function around a RW-anomaly, and leads to accurate or inaccurate scattering solutions in the two respective cases. The angles $\theta = \delta^5$ sample incidence directions which differ from normal incidence, at which the RW anomaly occurs, in angles of the order of 10^{-5} to 10^{-14}.

construction of the linear system to be inverted. The second challenge relates to the ill-conditioning of the system around RW-anomalies, which might also produce a loss of accuracy even if very accurate evaluations of G^q_κ are used, such as those arising from the Ewald or shifted Green function methods. The first of these difficulties is illustrated in Figure 3 (left), which displays the error in the energy balance criterion in a case in which the quasi-periodic Green function is computed by means of the Laplace-type integral method using equations (33) and (34)—in which the singular $1/\beta_m$ term has not explicitly been extracted—and by means of equations (33), (38) and (44)—which include singularity extraction. Figure 3 (right) displays results of two similar experiments, in both cases using singularity extraction, except that, in this case, the Ewald and shifted Green function representations are used to compute G^q_κ. These figures illustrate the benefits, irrespectively of the WSM formalism, that result from use of hybrid spatial/spectral representations which display explicitly both spatial poles and the finitely many terms which cause the divergence of G^q_κ at the RW-anomaly.

Difficulties related to system ill-conditioning around RW-anomalies, in turn, only emerge as high-accuracies are sought. As explained in Section 4, ill conditioning arises in these cases from the diagonal operator D^{-1} in equation (82), which blows up as the RW singularity is approached. In the two-dimensional example considered in the present section, D^{-1} diverges like $1/\sqrt{\Delta\theta}$ as $\Delta\theta \to 0$ resulting in matrices whose condition numbers only increase up to figures of the order of 10^8 in double precision arithmetic (Figure 4 right). Given that these values are not exceedingly large, a severe loss of accuracy is not evidenced (only a few digits are lost). However, the WSM regularization technique produces linear systems which are well-conditioned (at least for all the runs of the solvers and all the experiments presented in this article, see Figure 4 (right)) yielding a

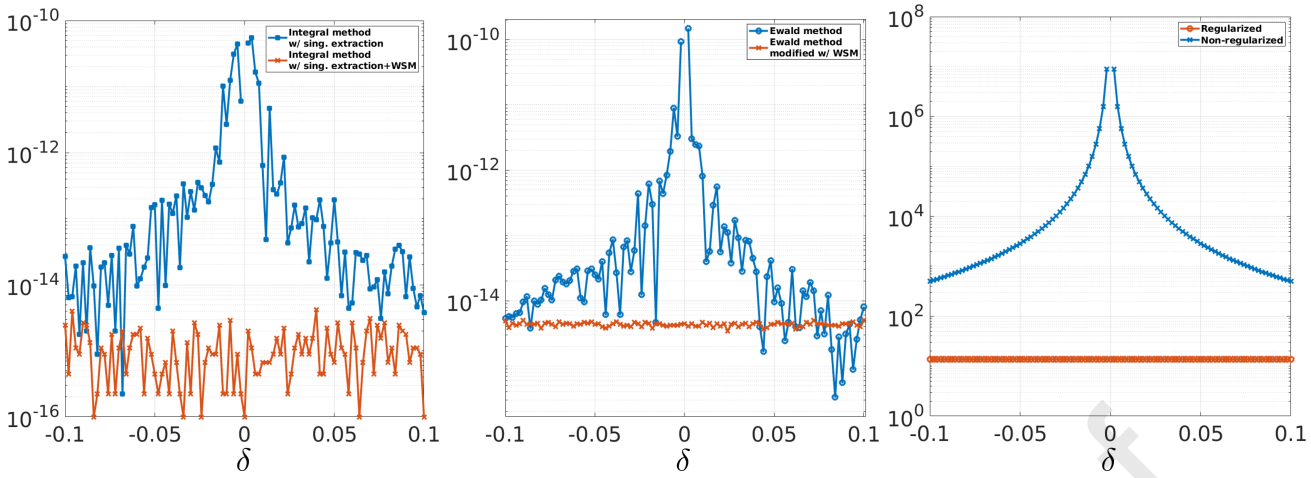

Figure 4: Energy balance errors (left and center) in the solution of the scattering problem depicted on the right image in Figure 2 on the basis of the Laplace-type integral method with singularity extraction, as proposed in this article (left), and Ewald methods (center), with and without WSM regularization. The angles $\theta = \delta^5$ sample incidence directions which differ from normal incidence in angles of the order of 10^{-5} to 10^{-14}. The right figure, which displays the condition numbers of the linear systems obtained on the basis of the Ewald method with and without WSM regularization, illustrates the effect of the WSM methodology on conditioning at and around RW-anomalies.

methodology which preserves the accuracy of the underlying method to evaluate G_κ^q and which can extend the solution to the RW-anomaly itself (Figure 4).

In what follows we demonstrate the validity and applicability of the proposed framework for a number of relevant examples.

5.3 Two dimensional simulations

The two-dimensional numerical experiments considered in this section illustrate the robustness of the overall methodology. Two arrays with periods 5λ and 10λ of impenetrable sound-soft elliptical cylinders are illuminated by a range of incidence angles sampling anomalous and non-anomalous configurations. In both cases 64 points are used to discretize each ellipse (Figure 2, right) and each series in the Ewald representation is truncated at $|m| < 40$. As can be clearly appreciated from the errors displayed in Figure 5, the overall accuracy of the methodology does not suffer at and around RW-anomalies. Scattering patterns for a particular incidence angle are displayed in Figure 2 (right).

5.4 Three dimensional simulations–Bi-periodic structures

In this section we first consider the problem of scattering of an incoming plane wave by a periodic array of impenetrable sound-soft tori (Figure 6, left). The results displayed in Tables 2 and 3 correspond to a lattice whose periodicity vectors are $\boldsymbol{v_1} = L(1, 0, 0)$ and $\boldsymbol{v_2} = L(\cos(\pi/3), \sin(\pi/3), 0)$ (a honeycomb structure) where the size of the period equals $L = \lambda$ and $L = 4\lambda$ respectively. The

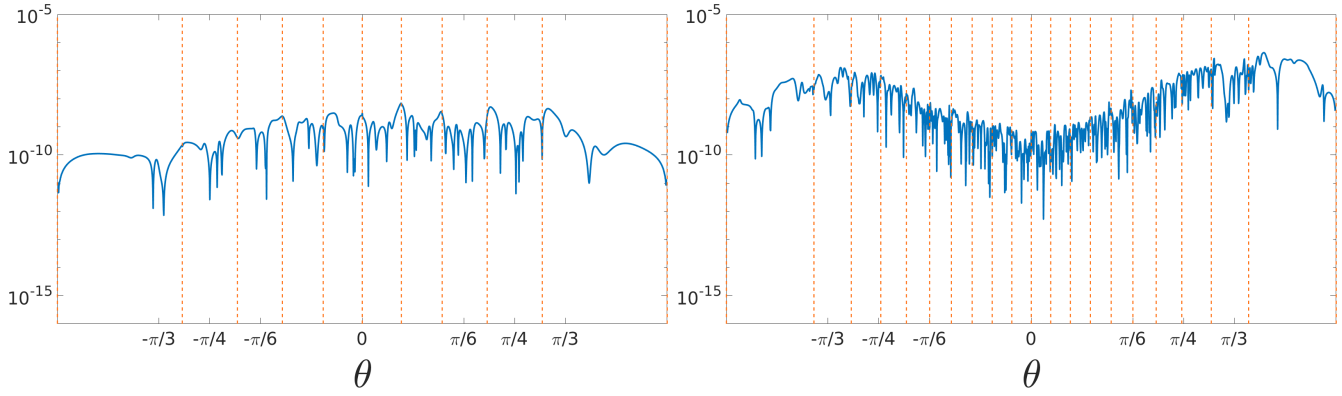

Figure 5: Energy balance error obtained from use of the Ewald method with WSM regularization, as a function of the incidence angle, for the scattering configurations depicted in the right image on Figure 2. The left and right graphs correspond to arrays of periods equal to 5λ and 10λ respectively.

wave impinges on the array with a propagation direction equal to

$$(\cos(\phi)\sin(\theta), \sin(\phi)\sin(\theta), -\cos(\theta)) \tag{91}$$

with $\phi = \pi/3$ and $\theta = \pi/6$ giving rise to an anomalous configuration in the example with largest period ($L = 4\lambda$). We use a global parametrization of the torus

$$\boldsymbol{x}(s,t) = (\cos(\pi s)(r\cos(\pi t) + R), \sin(\pi s)(r\cos(\pi t) + R), r\sin(\pi t)), \quad (s,t) \in [-1,1]^2$$

setting in both cases $R = L/4$ and $r = L/16$. Non-overlapping patches can be obtained by means of dyadic subdivisions of the square $[-1,1]^2$ and a proper re-scaling. High-order convergence can be appreciated from the displayed errors (Tables 2 and 3) as the discretization of the surface is refined (where the refinement is controlled with the number of patches and with the number of Chebyshev nodes in the u and v direction) as well as increasing the number of terms in the truncation of the series in the Ewald representation.

The second experiment conducted to test the robustness of the method around RW-anomalies resembles the one performed to produce Figures 5. We consider an impenetrable sound-soft crossed grating (that is, a grating for which the lattice directions lie at 90° from each other), whose boundary is parametrized by

$$\boldsymbol{x}(s,t) = \left(\frac{L}{2}s, \frac{L}{2}t, \frac{H}{2}\sin(\pi s)\sin(\pi t)\right), \quad (s,t) \in [-1,1]^2, \tag{92}$$

with period and height given by $L = 5\lambda$ and $H = \lambda$, and we compute the energy balance error for a range of 10,000 incidence directions (91) where the sample angles are given by $\theta_i = \arccos(i\pi/100)$, $\phi_j = 2\pi j/100$, $i,j = 0\ldots 99$. The unit-cell of the grating is divided in four non-overlapping patches (obtained from a single dyadic splitting of the parameter square $[-1,1]^2$ and a re-scaling of the parameters) and each is discretized with 16×16 Chebyshev grid points. The evaluation of the quasi-periodic Green function is performed by means of Ewald method truncating each of the required series with $\|\boldsymbol{m}\|_\infty < 20$. It can be clearly appreciated from Figure 6 (right) that high-accuracies are obtained irrespectively of the occurrence of RW-anomalies.

Patches	$N_u \times N_v$	N_{dis}	N_{tr}	EBC	A_0^+	Iterations	Time (s)
1	8×8	64	5	$6.3 \cdot 10^{-3}$	$4.7 \cdot 10^{-2}$	18	<1
		64	10	$6.3 \cdot 10^{-3}$	$4.7 \cdot 10^{-2}$	16	<1
		64	20	$6.3 \cdot 10^{-3}$	$4.7 \cdot 10^{-2}$	16	<1
	16×16	128	5	$8.0 \cdot 10^{-6}$	$4.4 \cdot 10^{-5}$	20	2
		128	10	$7.0 \cdot 10^{-6}$	$4.8 \cdot 10^{-5}$	18	3
		128	20	$7.0 \cdot 10^{-6}$	$4.8 \cdot 10^{-5}$	18	3
4	16×16	1024	5	$1.8 \cdot 10^{-6}$	$9.2 \cdot 10^{-6}$	15	7
		1024	10	$7.3 \cdot 10^{-8}$	$4.7 \cdot 10^{-7}$	14	13
		1024	20	$7.3 \cdot 10^{-8}$	$4.7 \cdot 10^{-7}$	14	36
	32×32	4096	5	$1.9 \cdot 10^{-6}$	$9.5 \cdot 10^{-6}$	15	103
		4096	10	$9.9 \cdot 10^{-9}$	0	14	198
		4096	20	$9.9 \cdot 10^{-9}$	Ref	14	568

Table 2: Convergence analysis for a periodic array of impenetrable tori arranged in a honeycomb structure with period equal to λ and for an incidence field for which the configuration is away from RW-anomalies. The quasi-periodic Green function was evaluated by means of the Ewald method where each infinite sum in the Ewald representation is truncated to $\|\boldsymbol{m}\|_\infty \leq N_{\text{tr}}$. See also Remark 5.

Patches	$N_u \times N_v$	N_{dis}	N_{tr}	EBC	A_0^+	Iterations	Time (s)
1	16×16	128	10	$2.4 \cdot 10^{-2}$	$2.6 \cdot 10^{-2}$	36	2
		128	20	$2.4 \cdot 10^{-2}$	$2.5 \cdot 10^{-2}$	35	3
		128	40	$2.4 \cdot 10^{-2}$	$2.5 \cdot 10^{-2}$	33	9
	32×32	1024	10	$4.4 \cdot 10^{-4}$	$7.8 \cdot 10^{-4}$	39	17
		1024	20	$2.1 \cdot 10^{-5}$	$1.9 \cdot 10^{-5}$	37	40
		1024	40	$2.2 \cdot 10^{-5}$	$1.9 \cdot 10^{-5}$	35	133
4	16×16	1024	10	$5.6 \cdot 10^{-4}$	$1.1 \cdot 10^{-3}$	32	18
		1024	20	$5.8 \cdot 10^{-5}$	$8.4 \cdot 10^{-5}$	29	42
		1024	40	$5.6 \cdot 10^{-5}$	$8.5 \cdot 10^{-5}$	28	133
	32×32	4096	10	$3.6 \cdot 10^{-4}$	$3.7 \cdot 10^{-4}$	29	268
		4096	20	$1.4 \cdot 10^{-6}$	$7.9 \cdot 10^{-7}$	26	638
		4096	40	$1.8 \cdot 10^{-8}$	Ref	24	2105

Table 3: Convergence analysis for a periodic array of impenetrable tori arranged in a honeycomb structure with period equal to 4λ under normal incidence, which gives rise to a RW anomaly. The anomaly was treated here by means of the WSM method. Truncations to $\|\boldsymbol{m}\|_\infty \leq N_{\text{tr}}$ were used for the WSM-modified Ewald summation method to obtain the highly accurate results displayed; see also Remark 5.

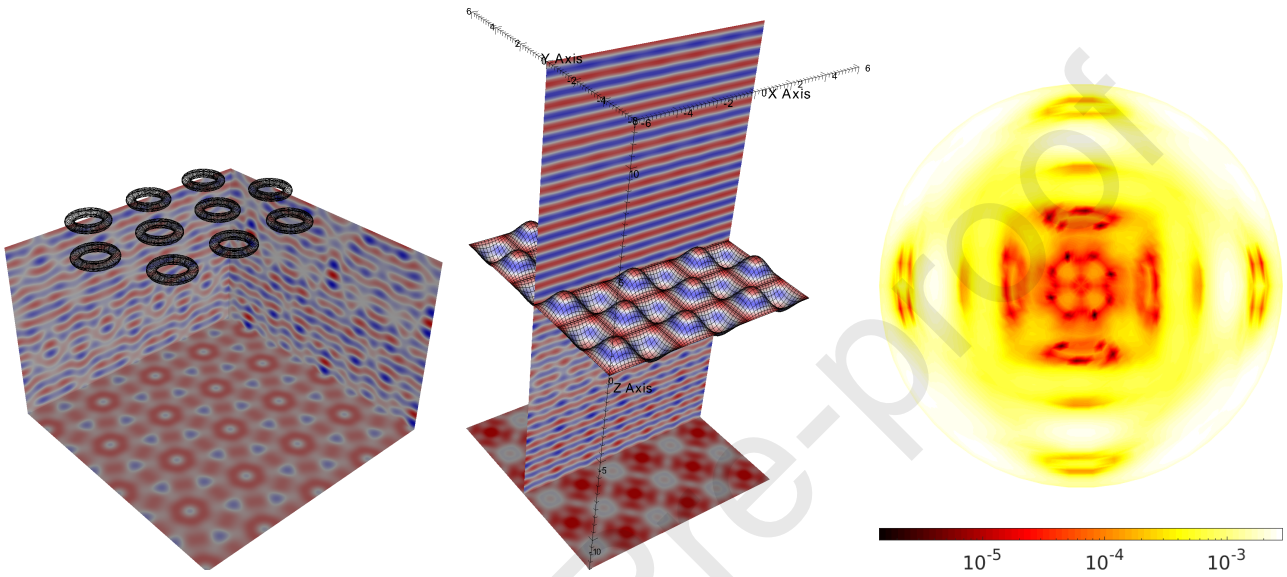

Figure 6: Real part of the total field scattered by an array of impenetrable tori arranged in a honeycomb structure (left) and by a bi-sinusoidal transmission crossed grating (center). The image on the right displays the energy balance error for a periodic crossed grating with period equal to 5λ as a function of the projection $(\cos(\phi)\sin(\theta), \sin(\phi)\sin(\theta))$ of the incidence direction in equation (91), some of which give rise to RW anomalies. For the latter case, the unit-cell of the grating is divided in four non-overlapping patches (obtained from a single dyadic splitting of the parameter square $[-1,1]^2$ and a re-scaling of the parameters) and each is discretized with 16×16 Chebyshev grid points. The evaluation of the quasi-periodic Green function was performed by means of Ewald method, truncating each of the required series to $\|\boldsymbol{m}\|_\infty < 20$; see also Remark 5. The WSM regularization formulation was used for these test cases for all near-RW configuration (which are defined here by the condition "$|\beta_{\boldsymbol{m}}| < 0.1$ for some $\boldsymbol{m}$").

Patches	$N_u \times N_v$	N_{dis}	N_{tr}	EBC	A_0^+	Iterations	Time (s)
4	8×8	256	10	$3.8 \cdot 10^{-3}$	$9.8 \cdot 10^{-3}$	32	2
		256	20	$2.4 \cdot 10^{-3}$	$9.8 \cdot 10^{-3}$	35	5
		256	40	$2.4 \cdot 10^{-3}$	$9.8 \cdot 10^{-3}$	33	9
	16×16	1024	5	$3.2 \cdot 10^{-5}$	$9.8 \cdot 10^{-5}$	32	32
		1024	10	$4.0 \cdot 10^{-6}$	$1.4 \cdot 10^{-6}$	32	80
		1024	20	$3.9 \cdot 10^{-6}$	$1.4 \cdot 10^{-6}$	32	255
	32×32	4096	5	$2.0 \cdot 10^{-4}$	$2.0 \cdot 10^{-4}$	30	212
		4096	10	$2.7 \cdot 10^{-10}$	$1.2 \cdot 10^{-10}$	19	720
		4096	20	$2.7 \cdot 10^{-10}$	Ref	19	1164

Table 4: Convergence analysis for a transmission crossed-grating with period equal to 2λ under normal incidence (an RW anomalous configuration). Truncations of the form $\|\boldsymbol{m}\|_\infty \leq N_{\text{tr}}$ of the modified Ewald summation method are used to obtain highly accurate results; see also Remark 5.

Finally we consider the convergence properties of the methodology for a transmission grating. In this case, the propagation domain $\Omega = \mathbb{R}^3$ having two subregions with constant refractive indexes $n_0 = 1$ and $n_1 = 1.25$ (Figure 6, center); the boundary between the two is parametrized by the mapping (92) where the period $L = 2\lambda_0$ (two wavelengths of the domain with refractive index $n_0 = 1$). Under normal incidence, this configuration gives rise to RW-anomalies in both domains (there are, in each set, 4 indexes $\boldsymbol{m}$ such that $\beta_{\boldsymbol{m}}(n_j k) = 0$, $j = 0, 1$). As can be clearly appreciated in Table 4, very high accuracies are obtained for the finest discretization and results with a small number of correct digits can be obtained in a few seconds.

5.5 Linear periodic arrays in three dimensional space

This section illustrates the applicability of the ideas developed in this article to the simulation of three-dimensional periodic structures with a single direction of periodicity. In order to obtain highly-accurate evaluations of G_κ^q we utilize the shifted Green function representation (58) which yields highly accurate results in fast computing times, in contrast to the Ewald method which has an erratic behavior in this context [12], and which, even when accurate, as it is for small values of $|\boldsymbol{x}^\perp|$, does not present a major advantage in terms of speed as in the bi-periodic case considered in the previous section. The Laplace-type integral method was not used either since it becomes costly due to the evaluation of Bessel functions with complex argument. Perhaps, in part, for these reasons, these type of configurations have received much less attention in the computational physics literature than their well-known bi-periodic relatives. The only $d_\Lambda = 1$, $d = 3$ problems of which we are aware are computations of eigenmodes for twisted waveguides on the basis of either approximate models [41] or finite-difference methods in time-domain (FDTD) [53]. The contributions [11, 29, 46, 51] consider linear arrays of spheres but they also focus on the study of guided modes in the periodic structure rather than the simulation of a wave-scattering process. To the best of our knowledge, the numerical simulations presented in what follows are the first high-order accurate numerical simulations ever produced for linear arrays in three-dimensional space.

We consider first the scattering of an impenetrable, sound-soft, double-helical structure comprised of two "twisted" cylinders (Figure 7) and compute the energy balance error for several discretization levels and a number of finite truncations of the shifted Green function represen-

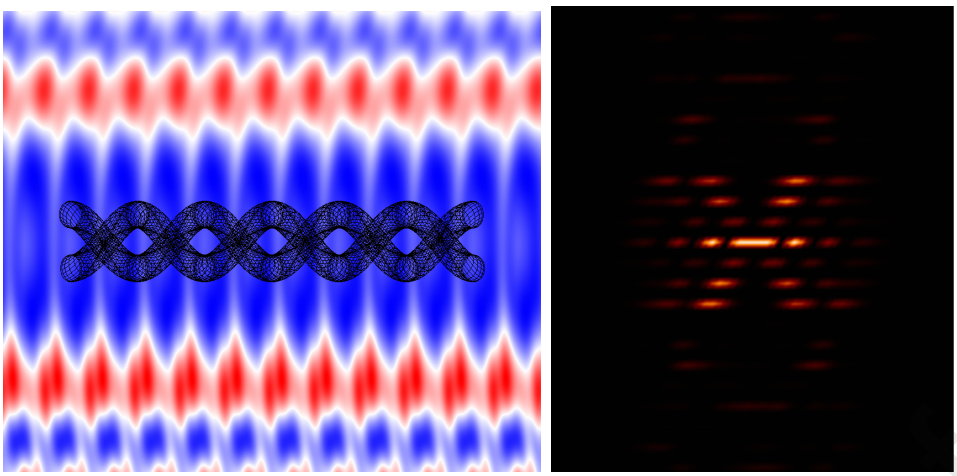

Figure 7: Left: Twisted double-helical surface structure of period 5λ illuminated by a plane wave with incidence direction given by (91) with $\phi = 0$ and $\theta = \pi/6$. The total-field intensity pattern, which was obtained by means of the shifted Green function method, is displayed on a plane parallel to the periodicity direction located 50 wavelengths behind the double helix structure. Right: Diffraction pattern (far field behind the double helix) obtained for an array of spheres located along two helical curves, which emulates the arrangement of phosphorus atoms in DNA molecules. The simulated pattern resembles closely the X-ray crystallography experimental results that allowed the discovery of the double-helical structure of DNA in the famous "Photo 51"—that can be easily found on the internet, but for which we were not able to find a published reference. When comparing the right image to the actual Photo 51 a mismatch can be seen at the center of the diffraction pattern: the experimental data does not contain the bright central line that is clearly visible on the right-hand image above. This is a feature of the experimental setup, which used a filter to occlude the intense line to avoid overexposure of the X-Ray photographic film.

tation (58). Each infinite helix is obtained from an appropriate rotation around the x_1-axis of the globally-parametrized surface

$$\boldsymbol{x}(s,t) = C(s) + r\cos(t)\hat{\boldsymbol{e_2}}(s) + r\sin(t)\hat{\boldsymbol{e_3}}(s), \quad s \in \mathbb{R}, t \in [0, 2\pi] \tag{93}$$

where $C(s) = (R\sigma s, R\cos(s), R\sin(s))$ is a parametrization of a helical curve with radius R and slope σ, where r is the inner-radius of the twisted cylinder and $\hat{\boldsymbol{e_2}}$ and $\hat{\boldsymbol{e_3}}$ are the normal and bi-normal unit vectors of the Frenet reference frame of the curve C. The subdivision into patches required by the rectangular integration methodology can be obtained by means of dyadic subdivisions of $[-1, 1]^2$ and proper rescalings. For the examples considered in Tables 5 and 6 we have set $r = \lambda/2$ and $R = \lambda$ in equation (93). The slope, in turn, is $\sigma = 5\lambda/(2\pi R)$ yielding a period equal to 5λ. In both cases the incident wave has a propagation direction given by equation (91) with $\phi = 0$ and $\theta = \pi/6$ for Table 5 (a non-anomalous configuration) and $\theta = 10^{-8}$ (very close to an RW-anomaly) for Table 6. (The case $\theta = 0$ can be treated by means of the WSM method without difficulty.) The results displayed in those tables demonstrate the excellent convergence properties of the shifted Green function in conjunction with the rectangular integration method away from and around RW-anomalies.

Patches	$N_u \times N_v$	N_{dis}	N	EBC	Iterations	Time (s)
4	16×16	1024	2	$1.4 \cdot 10^{-2}$	44	26.52
		1024	4	$1.3 \cdot 10^{-4}$	42	27.31
		1024	8	$5.2 \cdot 10^{-5}$	40	28.88

Table 5: Convergence analysis for a double-helix structure (Figure 7) of period 5λ using a fixed number N_{dis} of discretization points. The incidence direction is given by (91) with $\phi = 0$ and $\theta = \pi/6$ (not an RW-anomaly). The quasi-periodic Green function is evaluated by means of truncations of the shifted Green function representation (58) with $j = 8$ and $h = \lambda/2$. In this table, the sum over the spatial lattice in (58) (G_j^q in Equation (56)) is truncated to $|m| \leq N$ terms; see also Remark 5.

Patches	$N_u \times N_v$	N_{dis}	N	EBC	Iterations	Time (s)
16	16×16	4096	2	$4.4 \cdot 10^{-3}$	39	424.73
		4096	4	$1.1 \cdot 10^{-5}$	39	441.23
		4096	8	$6.9 \cdot 10^{-7}$	39	461.32

Table 6: Convergence analysis for a double-helix structure (Figure 7) of period 5λ. The incidence direction is given by (91) where $\phi = 0$ and $\theta = 10^{-8}$, very close to an RW-anomaly (which occurs at $\theta = 0$). The quasi-periodic Green function is evaluated by means of truncations of the shifted Green function representation (58) with $j = 8$ and $h = \lambda/2$. In this table, the sum over the spatial lattice in (58) (G_j^q, Equation (56)) is truncated to $|m| \leq N$ terms; see also Remark 5.

6 Conclusions

This paper studied the major challenges encountered by classical methods based on quasi-periodic Green functions for the simulation of wave-scattering by periodic media around RW-anomalies, which are observed in both two- and three-dimensional problems, and which are pervasive in the most challenging three-dimensional case. Through the concept of hybrid spatial/spectral representations, this contribution introduced a framework, the Woodbury-Sherman-Morrison methodology, to explain and bypass the problems presented by these singularities irrespectively of the underlying geometry of the scattering structure. As a result, fast and robust numerical solvers were obtained and applied to the simulation of acoustic wave-scattering by various two and three dimensional periodic structures with a variety of boundary conditions. The errors and times presented in this contribution render the software developed for this article among the fastest and most accurate and available to date for the configurations considered.

Acknowledgements

This work was supported by NSF and AFOSR through contracts DMS-1714169 and FA9550-15-1-0043, and by the NSSEFF Vannevar Bush Fellowship under contract number N00014-16-1-2808.

A Energy balance criterion

The principle of conservation of energy provides, under certain circumstances, a valuable indicator of the accuracy of a numerical methods for periodic structures. Even though the exact (or highly-accurate) verification of a conservation principle does not guarantee in general the convergence of the method, it provides a good estimator of the overall accuracy of the algorithm, specially when accompanied by other criteria, such as resolution analysis. In the wave-scattering by periodic (non-absorbing) media the relevant conservation principle follows from Green's second identity [43]. The following section presents a derivation of the energy-balance criterion for scattering by linear arrays in three-dimensional space which we have not found elsewhere. Other energy balance relations can be found e.g. in [43].

A.1 Scattering by linear arrays in three dimensional space, $d_\Lambda = 1$, $d = 3$

This section presents a derivation of the energy balance criterion for "linear" periodic structures which, like the ones considered in Section 5.5, consist of surfaces or arrays of impenetrable particles having periodicity along the x_1 axis. We assume that the scattering structure is contained within the cylinder $\Omega_M = \{\boldsymbol{x} \in \mathbb{R}^3 : x_2^2 + x_3^2 < M^2\}$ for some $M > 0$. Then, selecting $\rho > M$ and applying Green's second identity in Ω_M we have

$$0 = \int\limits_{\partial B(0,\rho)} \left(\overline{u} \frac{\partial u}{\partial \nu} - u \frac{\partial \overline{u}}{\partial \nu} \right) dS. \tag{94}$$

Now, writing $u = u^{\mathrm{s}} + u^{\mathrm{inc}}$ and replacing u^{s} by its corresponding Rayleigh expansion (26) it follows that

$$0 = \sum_{m\in\mathbb{Z}} \int\limits_{|\boldsymbol{x}^\perp|=\rho} \left(\overline{U_m} \frac{\partial U_m}{\partial \nu} - U_m \frac{\partial \overline{U_m}}{\partial \nu} \right) + 2\mathrm{i}\,\mathrm{Im} \left(\int\limits_{|\boldsymbol{x}^\perp|=\rho} \mathrm{e}^{\mathrm{i}\boldsymbol{\beta}\cdot\boldsymbol{x}^\perp} \frac{\partial U_0}{\partial \nu} - U_0 \frac{\partial \mathrm{e}^{\mathrm{i}\boldsymbol{\beta}\cdot\boldsymbol{x}^\perp}}{\partial \nu} \right). \tag{95}$$

For indexes m for which $\beta_m^2 = \kappa^2 - \alpha_m^2 > 0$, the functions U_m are solutions of the Helmholtz equation in two dimensional space satisfying Sommerfeld's radiation condition and therefore they can be expanded in the form

$$U_m(x_2, x_3) = \sum_{\ell\in\mathbb{Z}} u_\ell^{(m)} H_\ell^{(1)}(\beta_m |\boldsymbol{x}^\perp|) \mathrm{e}^{\mathrm{i}\ell\theta}, \tag{96}$$

where $H_\ell^{(1)}$ is the Hankel's function of the first kind of order ℓ and θ is such that $x_2 = |\boldsymbol{x}^\perp| \cos\theta$ and $x_3 = |\boldsymbol{x}^\perp| \sin\theta$. A similar expression for the factor $\mathrm{e}^{\mathrm{i}\boldsymbol{\beta}\cdot\boldsymbol{x}^\perp}$ of the incoming wave can be obtained by means of the Jacobi-Anger's expansion [16]

$$\mathrm{e}^{\mathrm{i}\boldsymbol{\beta}\cdot\boldsymbol{x}^\perp} = \sum_{\ell\in\mathbb{Z}} \mathrm{i}^\ell \mathrm{e}^{-\mathrm{i}\ell\tilde{\theta}} J_\ell(|\boldsymbol{\beta}||\boldsymbol{x}^\perp|) \mathrm{e}^{\mathrm{i}\ell\theta}, \tag{97}$$

where $\tilde{\theta}$ is such that $\boldsymbol{\beta} = |\boldsymbol{\beta}|(\cos\tilde{\theta}, \sin\tilde{\theta})$ and J_ℓ is the Bessel's function of the first kind of order ℓ. Using the orthogonality of the exponentials $\mathrm{e}^{i\ell\theta}$ in $L^2(\partial B(0,\rho))$ and the relations for the Wronskians [19, Eq. 10.5.1-5]

$$W(H_\ell^{(1)}, \overline{H_\ell^{(1)}})(z) = -\frac{4i}{\pi z}, \quad W(H_\ell^{(1)}, J_\ell)(z) = -\frac{2i}{\pi z},$$

we have

$$\int\limits_{|\boldsymbol{x}^{\perp}|=\rho} \left(\overline{U_m} \frac{\partial U_m}{\partial \nu} - U_m \frac{\partial \overline{U_m}}{\partial \nu} \right) = 8\mathrm{i} \sum_{\ell \in \mathbb{Z}} |u_n^{(m)}|^2 \tag{98}$$

and

$$\left(\int\limits_{|\boldsymbol{x}^{\perp}|=\rho} \mathrm{e}^{\mathrm{i}\boldsymbol{\beta}\cdot\boldsymbol{x}^{\perp}} \frac{\partial U_0}{\partial \nu} - U_0 \frac{\partial \mathrm{e}^{\mathrm{i}\boldsymbol{\beta}\cdot\boldsymbol{x}^{\perp}}}{\partial \nu} \right) = 4\mathrm{i} \sum_{\ell \in \mathbb{Z}} u_\ell^{(0)} \mathrm{i}^\ell \mathrm{e}^{\mathrm{i}\ell\tilde{\theta}}. \tag{99}$$

Note that these expressions are independent ρ. In contrast, for the indexes m such that $\beta_m^2 = \kappa^2 - \alpha_m^2 < 0$, U_m decays exponentially fast as $\rho \to \infty$ and therefore, the corresponding integrals involving U_m in that equation do not produce a contribution in the limit. The energy balance criterion for impenetrable periodic structures with $d_\Lambda = 1$ in three dimensional space,

$$\sum_{m \in U} \left(\sum_{\ell \in \mathbb{Z}} |u_\ell^{(m)}|^2 \right) = -\mathrm{Im} \left(\sum_{\ell \in \mathbb{Z}} \mathrm{e}^{\mathrm{i}\ell(\tilde{\theta}-\pi/2)} u_\ell^{(0)} \right), \tag{100}$$

is thus obtained.

References

[1] E. Akhmetgaliyev, O. P. Bruno, et al. "Regularized integral formulation of mixed Dirichlet-Neumann problems". In: *Journal of Integral Equations and Applications* 29.4 (2017), pp. 493–529.

[2] T. Arens et al. "Analysing Ewald's method for the evaluation of Green's functions for periodic media". In: *IMA Journal of Applied Mathematics* 78.3 (2013), pp. 405–431.

[3] O. P. Bruno and B. Delourme. "Rapidly convergent two-dimensional quasi-periodic Green function throughout the spectrum–including Wood anomalies". In: *Journal of Computational Physics* 262 (2014), pp. 262–290.

[4] O. P. Bruno and A. G. Fernandez-Lado. "Rapidly convergent quasi-periodic Green functions for scattering by arrays of cylinders—including Wood anomalies". In: *Proc. R. Soc. A* 473.2199 (2017), p. 20160802.

[5] O. P. Bruno and E. Garza. "A Chebyshev-based rectangular-polar integral solver for scattering by general geometries described by non-overlapping patches". In: *arXiv preprint arXiv:1807.01813* (2018).

[6] O. P. Bruno and M. C. Haslam. "Efficient high-order evaluation of scattering by periodic surfaces: deep gratings, high frequencies, and glancing incidences". In: *JOSA A* 26.3 (2009), pp. 658–668.

[7] O. P. Bruno and M. C. Haslam. "Efficient high-order evaluation of scattering by periodic surfaces: vector-parametric gratings and geometric singularities". In: *Waves in Random and Complex Media* 20.4 (2010), pp. 530–550.

[8] O. P. Bruno and M. Maas. "Shifted equivalent sources and FFT acceleration for periodic scattering problems, including Wood anomalies". In: *Journal of Computational Physics* (2018).

[9] O. P. Bruno et al. "Superalgebraically convergent smoothly windowed lattice sums for doubly periodic Green functions in three-dimensional space". In: *Proc. R. Soc. A* 472.2191 (2016), p. 20160255.

[10] O. P. Bruno et al. "Three-dimensional quasi-periodic shifted Green function throughout the spectrum, including Wood anomalies". In: *Proc. R. Soc. A* 473.2207 (2017), p. 20170242.

[11] E. N. Bulgakov and D. N. Maksimov. "Optical response induced by bound states in the continuum in arrays of dielectric spheres". In: *JOSA B* 35.10 (2018), pp. 2443–2452.

[12] F. Capolino, D. Wilton, and W. Johnson. "Efficient computation of the 3D Green's function for the Helmholtz operator for a linear array of point sources using the Ewald method". In: *Journal of Computational Physics* 223.1 (2007), pp. 250–261. ISSN: 0021-9991. DOI: http://dx.doi.org/10.1016/j.jcp.2006.09.013. URL: http://www.sciencedirect.com/science/article/pii/S0021999106004359.

[13] H. Childs et al. "VisIt: An End-User Tool For Visualizing and Analyzing Very Large Data". In: *High Performance Visualization–Enabling Extreme-Scale Scientific Insight*. Oct. 2012, pp. 357–372.

[14] M. H. Cho. "Spectrally-accurate numerical method for acoustic scattering from doubly-periodic 3D multilayered media". In: *arXiv preprint arXiv:1806.03813* (2018).

[15] D. Colton and R. Kress. *Integral equation methods in scattering theory*. Vol. 72. SIAM, 2013.

[16] D. Colton and R. Kress. *Inverse acoustic and electromagnetic scattering theory*. Vol. 93. Springer Science & Business Media, 2012.

[17] A. Darweesh et al. "The role of Rayleigh-Wood anomalies and surface plasmons in optical enhancement for nano-gratings". In: *Nanomaterials* 8.10 (2018), p. 809.

[18] R. Denlinger et al. "A fast summation method for oscillatory lattice sums". In: *Journal of Mathematical Physics* 58.2 (2017), p. 023511.

[19] N. DLMF. "Digital Library of Mathematical Functions". In: *WJ Olver, AB Olde Daalhuis, DW Lozier, BI Schneider, RF Boisvert, CW Clark, BR Miller and BV Saunders, eds* (2017).

[20] P. P. Ewald. "Die Berechnung optischer und elektrostatischer Gitterpotentiale". In: *Annalen der physik* 369.3 (1921), pp. 253–287.

[21] V. Frayssé et al. "A set of GMRES routines for real and complex arithmetics". In: *Tech. Rep. TR/PA/97/49, CERFACS, France* (1997).

[22] K.-Y. Kim et al. "Slow-light effect via Rayleigh anomaly and the effect of finite gratings". In: *Optics letters* 40.22 (2015), pp. 5339–5342.

[23] H. Kurkcu, N. Nigam, and F. Reitich. "An integral representation of the Green function for a linear array of acoustic point sources". In: *Journal of Computational Physics* 230.8 (2011), pp. 2838–2856.

[24] H. Kurkcu and F. Reitich. "Stable and efficient evaluation of periodized Green's functions for the Helmholtz equation at high frequencies". In: *Journal of Computational Physics* 228.1 (2009), pp. 75–95.

[25] A. Kustepeli and A. Q. Martin. "On the splitting parameter in the Ewald method". In: *IEEE Microwave and Guided Wave Letters* 10.5 (May 2000), pp. 168–170. ISSN: 1051-8207. DOI: 10.1109/75.850366.

[26] J. Lai, M. Kobayashi, and A. Barnett. "A fast and robust solver for the scattering from a layered periodic structure containing multi-particle inclusions". In: *Journal of Computational Physics* 298 (2015), pp. 194–208.

[27] C. M. Linton. "Lattice sums for the Helmholtz equation". In: *SIAM review* 52.4 (2010), pp. 630–674.

[28] C. M. Linton. "The Green's Function for the Two-Dimensional Helmholtz Equation in Periodic Domains". In: *Journal of Engineering Mathematics* 33.4 (May 1998), pp. 377–401. DOI: 10.1023/A:1004377501747. URL: https://doi.org/10.1023/A:1004377501747.

[29] C. M. Linton, V. Zalipaev, and I. Thompson. "Electromagnetic guided waves on linear arrays of spheres". In: *Wave Motion* 50.1 (2013), pp. 29–40.

[30] C. Linton and I. Thompson. "Resonant effects in scattering by periodic arrays". In: *Wave motion* 44.3 (2007), pp. 165–175.

[31] Y. Liu and A. H. Barnett. "Efficient numerical solution of acoustic scattering from doubly-periodic arrays of axisymmetric objects". In: *Journal of Computational Physics* 324 (2016), pp. 226–245.

[32] G. Lovat, P. Burghignoli, and R. Araneo. "Efficient evaluation of the 3-D periodic Green's function through the Ewald method". In: *IEEE Transactions on Microwave Theory and Techniques* 56.9 (2008), pp. 2069–2075.

[33] A. Maradudin et al. "Rayleigh and Wood anomalies in the diffraction of light from a perfectly conducting reflection grating". In: *Journal of Optics* 18.2 (2016), p. 024004.

[34] A. A. Maradudin and I. Simonsen. "Rayleigh and Wood anomalies in the diffraction of acoustic waves from the periodically corrugated surface of an elastic medium". In: *Low Temperature Physics* 42.5 (2016), pp. 354–360.

[35] A. Maurel et al. "Wood's anomalies for arrays of dielectric scatterers". In: *Journal of the European Optical Society-Rapid publications* 9 (2014).

[36] D. Maystre. "Theory of Wood's anomalies". In: *Plasmonics*. Springer, 2012, pp. 39–83.

[37] W. McLean and W. C. H. McLean. *Strongly elliptic systems and boundary integral equations*. Cambridge university press, 2000.

[38] J. A. Monro. "A super-algebraically convergent, windowing-based approach to the evaluation of scattering from periodic rough surfaces". PhD thesis. California Institute of Technology, 2008.

[39] D. Nicholls, C. Pérez-Arancibia, and C. Turc. "Sweeping preconditioners for the iterative solution of quasiperiodic Helmholtz transmission problems in layered media". In: *arXiv preprint arXiv:1809.05634* (2018).

[40] B. Nijboer and F. De Wette. "On the calculation of lattice sums". In: *Physica* 23.1-5 (1957), pp. 309–321.

[41] S. Nordebo et al. "On the natural modes of helical structures". In: *arXiv preprint arXiv:1502.00496* (2015).

[42] C. Perez-Arancibia et al. "Domain decomposition for quasi-periodic scattering by layered media via robust boundary-integral equations at all frequencies". In: *arXiv preprint arXiv:1801.09094* (2018).

[43] R. Petit and M. Cadilhac. "Electromagnetic theory of gratings: some advances and some comments on the use of the operator formalism". In: *J. Opt. Soc. Am. A* 7.9 (Sept. 1990), pp. 1666–1674. DOI: 10.1364/JOSAA.7.001666. URL: http://josaa.osa.org/abstract.cfm?URI=josaa-7-9-1666.

[44] W. H. Press et al. *Numerical recipes 3rd edition: The art of scientific computing*. Cambridge university press, 2007.

[45] S. Savoia et al. "Surface sensitivity of Rayleigh anomalies in metallic nanogratings". In: *Optics express* 21.20 (2013), pp. 23531–23542.

[46] R. Shore and A. Yaghjian. "Travelling electromagnetic waves on linear periodic arrays of lossless spheres". In: *Electronics Letters* 41.10 (2005), pp. 578–580.

[47] B. Simon. *A comprehensive course in analysis*. American Mathematical Society Providence, Rhode Island, 2015.

[48] I. Stevanoviæ and J. R. Mosig. "Periodic Green's function for skewed 3-D lattices using the Ewald transformation". In: *Microwave and Optical Technology Letters* 49.6 (2007), pp. 1353–1357.

[49] I. Stevanovic et al. "Integral-equation analysis of 3-D metallic objects arranged in 2-D lattices using the Ewald transformation". In: *IEEE Transactions on Microwave Theory and Techniques* 54.10 (2006), pp. 3688–3697.

[50] M. Tavakoli, Y. S. Jalili, and S. M. Elahi. "Rayleigh-Wood anomaly approximation with FDTD simulation of plasmonic gold nanohole array for determination of optimum extraordinary optical transmission characteristics". In: *Superlattices and Microstructures* 130 (2019), pp. 454–471.

[51] I. Thompson and C. M. Linton. "Guided surface waves on one-and two-dimensional arrays of spheres". In: *SIAM Journal on Applied Mathematics* 70.8 (2010), pp. 2975–2995.

[52] M. E. Veysoglu et al. "Polarimetric passive remote sensing of periodic surfaces". In: *Journal of Electromagnetic Waves and Applications* 5.3 (1991), pp. 267–280.

[53] J. L. Wilson et al. "Analysis of rapidly twisted hollow waveguides". In: *IEEE Transactions on Microwave Theory and Techniques* 57.1 (2009), p. 130.

Declaration of interests

☒ The authors declare that they have no known competing financial interests or personal relationships that could have appeared to influence the work reported in this paper.

☐The authors declare the following financial interests/personal relationships which may be considered as potential competing interests:

Declaration of Interests: NONE